Geoderma 449 (2024) 117009

Contents lists available at ScienceDirect

Geoderma

journal homepage: www.elsevier.com/locate/geoderma

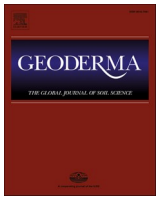

Factors controlling peat soil thickness and carbon storage in temperate peatlands based on UAV high-resolution remote sensing

Yanfei Li [a,*], Maud Henrion [a], Angus Moore [a], Sébastien Lambot [a], Sophie Opfergelt [a], Veerle Vanacker [a], François Jonard [b,1], Kristof Van Oost [a,1]

[a] Earth and Life Institute, Université catholique de Louvain, 1348 Louvain-la-Neuve, Belgium
[b] Earth Observation and Ecosystem Modelling Laboratory, Université de Liège, 4000 Liège, Belgium

ARTICLE INFO

Handling Editor: B. Minasny

Keywords:
Peatlands
Peat thickness
Carbon stock
Global warming
Thermal and multispectral remote sensing
UAV LiDAR

ABSTRACT

Peatlands store a large amount of carbon. However, peatlands are complex ecosystems, and acquiring reliable estimates of how much carbon is stored underneath the Earth's surface is inherently challenging, even at small scales. Here, we aim to establish links between the above- and below-ground factors that control soil carbon status, identify the key environmental variables associated with carbon storage, as well as to explore the potential for using Unmanned Aerial Vehicle (UAV) remote sensing for spatial mapping of peatlands. We combine UAVs equipped with Red-Green-Blue (RGB), multispectral, thermal infrared, and light detection and ranging (LiDAR) sensors with ground-penetrating radar (GPR) technology and traditional field surveys to provide a comprehensive, 3-dimensional mapping of a peatland hillslope-floodplain landscape in the Belgian Hautes Fagnes. Our results indicate that both peat thickness and soil organic carbon (SOC) stock (top 1 m) are spatially heterogeneous and that the contributions from the surface topography to peat thickness and SOC stock varied from micro- to macro-scales. Peat thickness was more strongly controlled by macro-topography ($R^2 = 0.46$) than SOC stock, which was more influenced by micro-topography ($R^2 = 0.21$). Current vegetation had little predictive power for explaining their spatial variability. Additionally, the UAV data provided accurate estimates of both peat thickness and SOC stock, with RMSE and R^2 values of 0.16 m and 0.85 for the peat thickness, and 59.25 t/ha and 0.85 for the SOC stock. However, similar performance can already be achieved by using only topographical data from the LiDAR sensor (for peat thickness) and a combination of peat thickness and topography (for SOC stock) as predictor variables. Our study bridges the gap between surface observations and the hidden carbon reservoir below. This not only allows us to improve our ability to assess the spatial distribution of SOC stocks, but also contributes to our understanding of the environmental factors associated with SOC storage in these highly heterogeneous landscapes, providing insights for environmental science and climate projections.

1. Introduction

Peatlands (including mires, raised bogs, and fens) are areas where an accumulation of dead plant material occurs in water-logged and anoxic conditions over centuries to millennia, forming thick layers of partially decomposed organic matter known as peat (Gorham, 1957; Moore, 1989). Although peatlands cover less than 4 % of the Earth's land surface (Xu et al., 2018), they store around 600 Gt of carbon (Yu et al., 2010), which is approximately one-third of the total soil carbon pool (Dargie et al., 2017) and twice the amount of carbon stored in the biomass of global forest ecosystems (Pan et al., 2011). However, peatlands are vulnerable to both anthropogenic and natural disturbances such as land use/cover change (Tonks et al., 2017; Wang et al., 2023), wildfires (Wilkinson et al., 2023), and climate change (Leng et al., 2019;

Abbreviations: UAV, Unmanned Aerial Vehicle; RGB, Red-Green-Blue; LiDAR, light detection and ranging; GPR, ground-penetrating radar; 3D, three dimensions; RS, remote sensing; EMI, electromagnetic induction; GCPs, ground control points; DSM, Digital Surface Model; DTM, Digital Terrain Model; CHM, Canopy Height Model; TWI, Terrain Wetness Index; OSAVI2, Optimized Soil Adjusted Vegetation Index 2; BD, soil bulk density; SOM, soil organic matter; SOC, soil organic carbon; TN, total nitrogen.

* Corresponding author at: Place Louis Pasteur 3, 1348 Louvain-la-Neuve, Belgium.
E-mail address: yanfei.li@uclouvain.be (Y. Li).

[1] These authors are co-last authors.

https://doi.org/10.1016/j.geoderma.2024.117009
Received 15 June 2024; Received in revised form 15 August 2024; Accepted 15 August 2024
Available online 23 August 2024

Wang et al., 2018). For example, recent studies have suggested that global warming and associated changes in hydrology have the potential to accelerate soil heterotrophic respiration (e.g., Dorrepaal et al. (2009), Huang et al. (2021), Nissan et al. (2023), Zhao et al. (2017)). In Europe, an estimated 20 % of raised bogs (i.e., ombrotrophic bogs, fed by precipitation) are threatened by climate change and drainage, resulting in the release of approximately 24.2 Pg C into the atmosphere (van der Velde et al., 2021). Although an in-depth understanding of carbon dynamics within peatlands is crucial for understanding global change, research is confronted with several challenges in acquiring reliable estimates of how much carbon is stored underneath the surface of peatlands (Loisel et al., 2017; Minasny et al., 2019; Yu, 2012).

The spatial distribution of soil organic carbon (SOC) within peatlands is affected by complex interactions between environmental factors such as topography (Parry and Charman, 2013), hydrological conditions (Crezee et al., 2022), degradation/restoration trajectories (Krüger et al., 2021; Orella et al., 2022) and vegetation species and density (Dieleman et al., 2017). Topography is an especially important factor governing peatland development (Graniero and Price, 1999) because it controls the movement of water, sediment, and biogeochemical fluxes from the hillslope to the catchment scale (Li et al., 2018). Water table dynamics impose a strong influence on organic carbon mineralization rates because peat accumulation occurs under waterlogged and anaerobic conditions, whereas a lowering of the water table brings in more oxygen, which favours microbial decomposition (Fenner and Freeman, 2011). Furthermore, the spatial distribution of peat-forming species, such as *Sphagnum* mosses that produce decay-resistant litter (Dorrepaal et al., 2005; Rydin, 2013), and vascular plants, which regulate ecosystem water, carbon, and nutrient cycles (van der Velde et al., 2021), is controlled by complex hummock-hollow microtopography (Harris and Baird, 2019). Currently, understanding the interplay between above- and below-ground factors in the three dimensions (3D) of peatland landscapes is far from complete, which makes it difficult to identify the factors affecting carbon variability.

Reliable assessment of carbon storage is crucial for understanding the role of peatlands in the global carbon cycle and for providing insights into conservation and management strategies. Traditionally, researchers have relied on intensive field sampling (mainly probing and coring) to measure peat thickness and calculate the carbon stock at a given location. However, this approach is labour-intensive, time-consuming, and has the risk of disturbing sensitive habitats and species. Remote sensing (RS) enables the collection of land surface data in a spatially continuous manner at various spatio-temporal scales (Czapiewski and Szumińska, 2022; Jonard et al., 2018). So far, much effort has been made to map peatland extent (Dargie et al., 2017), peatland degradation status (Carless et al., 2019), and floristic composition (Harris et al., 2015), whereas only 11 % of these studies estimated carbon stock (Minasny et al., 2019). This is because peat deposits are hidden below the surface, and conventional RS techniques do not provide direct information on subsurface properties. To address this problem, various studies have first attempted to produce reliable peat thickness maps. Kriging is commonly used for interpolating peat thickness from point measurements to larger scales (Akumu and McLaughlin, 2014; Jaenicke et al., 2008), however, it requires a large number of field observations. Spatial modelling can achieve moderate accuracy by combining information on terrain attributes (e.g., elevation, slope, and aspect) and other environmental covariates (e.g., the distance to the river) (Crezee et al., 2022; Holden and Connolly, 2011; Parry et al., 2012; Rudiyanto et al., 2016a). Ground geophysical methods such as ground-penetrating radar (GPR), electromagnetic induction (EMI), and portable gamma ray sensors have been shown to be the most precise and reliable tools in detecting peat soil thickness (Henrion et al., 2024; Koganti et al., 2023; Parry et al., 2014), and their integration with airborne platforms and LiDAR sensors has great potential in spatial mapping of peatlands (Carless et al., 2021; Deragon et al., 2022; Gatis et al., 2019; McClellan et al., 2017; Silvestri et al., 2019a; Silvestri et al., 2019b). The results can then be upscaled to the landscape scale by applying machine learning methods that consider multiple variables (e.g., precipitation seasonality, distance to the peatland margin and nearest drainage point, elevation, or Sentinel 1 A radar images) (Crezee et al., 2022; Fiantis et al., 2023). Most previous carbon storage estimates were based on models that incorporate a map of peat thickness predicted by satellite-derived topography and vegetation data, average peat carbon content, and average bulk density data from existing literature (Aitkenhead and Coull, 2016; Beilman et al., 2008; Chapman et al., 2009; Jaenicke et al., 2008; Rudiyanto et al., 2018; Rudiyanto et al., 2015; Vernimmen et al., 2020; Warren et al., 2017). However, this approach does not consider the spatial heterogeneity of peat properties, which can introduce considerable uncertainties in carbon inventory assessments (Anda et al., 2021).

Unmanned Aerial Vehicles (UAVs) are particularly well-suited for monitoring the dynamics and interactions within complex peatland ecosystems. The UAV technique has been successfully employed for peatland vegetation mapping (e.g., Beyer et al. (2019); Räsänen and Virtanen (2019); Räsänen et al. (2020)) and topography reconstruction (e.g., Czapiewski (2022); Lovitt et al. (2017)), whereas only a few studies have focused on peat soil thickness (Davenport et al., 2020) or carbon stock estimation (Fernandes et al., 2020). In a recent example, Lopatin et al. (2019) successfully utilized UAV-hyperspectral-derived vegetation attributes as proxies to evaluate the belowground carbon stock in conservative and anthropogenic peatlands, implying a strong linkage between surface- and sub-surface processes. Previous studies also demonstrated that microtopography has an impact on hydrologic conditions, biogeochemical processes, and exogenous processes, which in turn influence carbon distribution at small scales (Iseas et al., 2024; Shukla et al., 2023; Villa et al., 2019; Wang et al., 2023). For instance, Wang et al. (2021c) found that 56 % of the total SOC was stored in and under hummocks, although hummock microtopography only accounted for 30 % of their sedge peatland study area. Unmanned aerial vehicles equipped with LiDAR sensors have been demonstrated to be effective tools for reconstructing Digital Terrain Model/Canopy Height Model (DTM/CHM) at sub-centimetre resolution, making them valuable for characterizing microtopography (Shukla et al., 2023) and vegetation structure (Bates et al., 2021). However, little is known about the spatial scale needed to accurately represent microtopography and vegetation. In other words, although ultra-high-resolution sensing now provides information at unprecedented resolutions, the relevant spatial scales at which these patterns reflect underlying processes remain largely underexplored.

Currently, most studies tend to utilize a specific spatial scale level to study the relationship between environmental factors and peat depth or carbon storage within peatlands, which may ignore potentially important impacts at other scales. As Räsänen et al. (2020) stated, landscape elements such as vegetation, topography, and moisture exhibit variations across sub-centimeter to meter scales. While some spatial differences are visible at the centimetre-scale resolution, larger-scale gradients manifest themselves at macro-scales (e.g., Beucher et al. (2020); Harris et al. (2015)). Since SOC stock is controlled by biogeochemical processes operating at different spatial scales, it is necessary to explore these patterns in further detail. High-resolution UAV data offers the base conditions to perform multiresolution analysis (which provides multiple results for one indicator at multiple scales (Kalbermatten et al., 2012)).

In this study, we integrate UAV RS methods with GPR technology and traditional field surveys to gather a comprehensive 3D picture, ranging from the plant canopy to the bedrock, and apply these techniques in a peatland landscape in the Belgian Hautes Fagnes. Our overall objective is to improve our capacity to assess the spatial distribution of C stocks by providing insights into the factors controlling carbon storage in these highly heterogeneous landscapes. More specifically, our study aims to achieve three key objectives. First, we aim to characterize the spatial and vertical distribution of peat thickness and carbon stock.

Second, we aim to identify the factors controlling peat soil thickness and carbon stock spatial variability, whereby we focus specifically on a multiresolution analysis of metrics representing processes occurring both at the surface and in the subsurface. Lastly, we investigate the potential of mapping peat thickness and carbon stock using ultra-high-resolution data derived from UAV-borne sensors.

2. Materials and methods

2.1. Study site

The Belgian Hautes Fagnes plateau is part of the Stavelot-Venn Massif, situated in the eastern part of Belgium (Fig. 1a), with the highest point reaching 694 m above sea level (Goemaere et al., 2016). Due to the relatively high altitude, the plateau intercepts clouds and moist vapor from the Atlantic Ocean, resulting in a humid climate: often enveloped in mist and low clouds, and marked by strong winds and severe winters. The mean annual temperature is around 6.7 °C and the mean annual precipitation is about 1439.40 mm (Mormal and Tricot, 2004). In addition, many depressions caused by Lithalsas—permafrost mounds formed by ice segregation in mineral-rich soil that occur within the zone of discontinuous permafrost—were formed at an elevation of more than 500 m during the Younger Dryas (Pissart, 2003). These topographical, geomorphological, climatic, and lithological factors created favourable conditions for the development of peatlands (Goemaere et al., 2016).

The peatlands in this region predominantly comprise raised bogs, covering 3750 ha, which have formed since the Late Pleistocene (Frankard et al., 1998). Our study site (50.4948 N, 6.0520 E) is a peatland landscape with an area of 33 ha, located in the upper valley of the Hoëgne River in the Hautes Fagnes (Fig. 1a). It is characterized by a relatively steep topographic gradient, with a clear transition from a low-gradient plateau in the south to steep hillslopes and the fluvial valley and floodplain in the north (Sougnez and Vanacker, 2011). The site was drained and planted with spruce in 1914 and 1918. These spruce plantations were subsequently cleared between 2000 and 2016; since 2017, the site is under active restoration and hardwood species such as *Betula pubescens* and *Quercus robur* have been planted. Other natural dwarf shrubs and grasses such as *Calluna vulgaris, Vaccinium myrtillus, Molinia caerulea, Juncus acutus*, and peat mosses are also found in this area (Fig. 1b). There is a meteorological observation station (50.5113 N, 6.0746 E) 3.07 km away, where the Royal Meteorological Institute of Belgium records rainfall and air temperature every 10 min.

2.2. Soil sampling

Disturbed soil samples for chemical analysis (sections 2.3 and 2.4) were collected from 42 soil profiles along three evenly spaced transects parallel to the main slope between July 2022 and May 2023. In total, 298 soil samples were collected at depths ranging between 0 and 150 cm (Fig. 1a). The profile locations are representative of the site heterogeneity in vegetation and topography. After removing the litter horizon, soil samples were taken using four different methods (26 profiles with an Edelman auger, 2 profiles with a peat sampler, 6 manually inserted PVC tubes, and 8 soil profile pits) depending on the local soil conditions. We corrected soil compaction in the PVC cores by measuring the sampling depth in the field. In the soil profile pits, 54 undisturbed samples were taken at different depths with a 100 cm^3 Kopecky ring for the determination of the soil bulk density. The undisturbed soil samples were dried at 105 °C for 48 h to a constant mass. Soil bulk density (BD, g cm^{-3}) was then determined by dividing the oven-dried soil mass by the original sample volume. An Emlid Reach RS 2 GPS device with centimetric precision (with RTK technology) was used to record the position of the soil profiles. We also recorded the dominant vegetation type (Plunus et al., 2013). Peat soil thickness was measured in the soil pits and cores (n = 36). We complemented this dataset with data from Henrion et al. (2024) obtained from the same site and derived from GPR measurements (n = 148) and manual augering (11 peat depth observations). The GPR is used to infer soil composition and structure by detecting contrasts in the soil's electromagnetic properties (Doolittle,

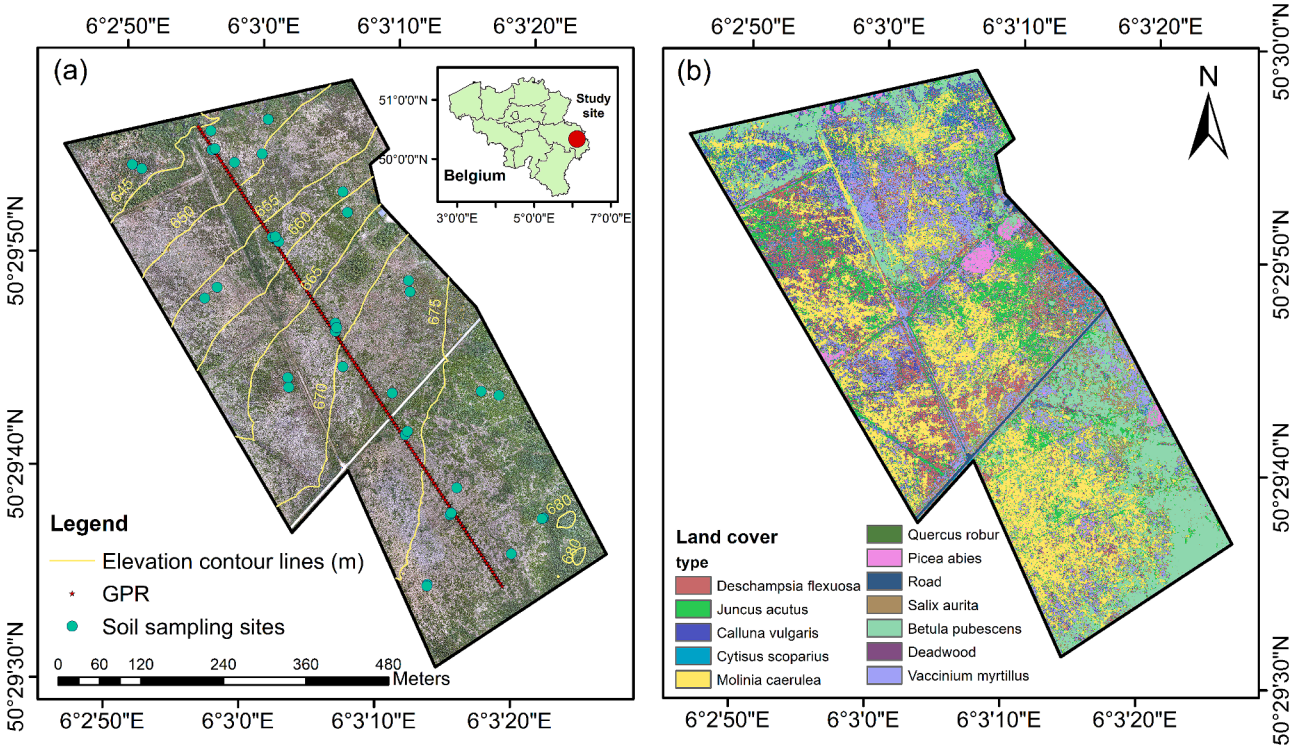

Fig. 1. Maps of field-sampling locations (a) and land cover types (b) in the study area. The land cover map was produced by a Random Forest model, using multi-sensor UAV data as predictors. For more information on land cover classification, see Table S1, Table S2, and Fig. S2 in the Appendix.

1987), such as the transition from the peat horizon to the mineral soil horizon (Wastiaux et al., 2000). In 2023, a GPR survey was conducted along the middle transect and peat thickness data from soil cores were collected at 5-meter intervals, resulting in a dataset of 148 observations of peat thickness (Henrion et al., 2024). Based on our statistical analysis, the GPR-derived peat thickness and soil coring observation show good consistency ($RMSE = 0.11$ m, Lin's concordance correlation coefficient $= 0.96$), therefore, the GPR data was also used as in-situ observations in this study.

2.3. Laboratory soil analysis

Disturbed soil samples including 112 samples that were air-dried and 186 samples that were oven-dried at 80 °C for 48 h (Dettmann et al., 2021), were crushed, ground, and sieved to pass through a mesh of 2 mm. Roots and litter were removed by tweezers during the pre-processing procedure. A subset of samples was analysed for soil organic matter (SOM), carbon and nitrogen elemental composition, and soil texture. The soil organic matter (SOM) content of 163 samples was determined by the Loss on Ignition (LOI) method at 550 °C in a muffle furnace for 12 h using ~1 g homogenized subsamples of the prepared soil. The LOI is commonly used to determine the organic matter content of peat soil (Crezee et al., 2022; Farmer et al., 2014; Hribljan et al., 2017; Rodriguez et al., 2021). The soil texture (clay-sized fraction, silt-sized fraction, sand-sized fraction) for a subset of 66 samples (air-dried) was measured by a Laser Diffraction Particle Size Analyzer (Model LS13 320; Beckman Coulter Inc., Fullerton, USA). Firstly, we selected a subsample of around 5 g using a sample splitter and transferred it to a beaker. Then we wet the sample with demineralized water and added 35 % hydrogen peroxide (H_2O_2) to break down and remove organic matter (Beuselinck et al., 1998). Afterwards, samples were treated with ultrasound. A total of one hundred and twelve reference soil samples (air-dried) were finely ground into powder for soil organic carbon (SOC) and total nitrogen content (TN) analysis (Carlo Erba EA1108 Analyzer, Fullerton, USA). After weighing ~5–15 mg homogenized individual subsamples, we added one drop of 5 % HCl to each sample to test the presence of inorganic carbon but found that no inorganic carbon was present in the 112 reference samples. We then used soil spectroscopy to estimate these parameters for the remaining samples (see below).

2.4. Spectroscopy measurements and modelling

All ground and sieved soil samples were scanned in the laboratory using an ASD FieldSpec 3 spectroradiometer in the VIS-NIR range (350–2500 nm) (Analytical Spectral Devices Inc., USA). We used the methods described in Zhao et al. (2023) to construct spectral prediction models and predicted SOC, total nitrogen, and texture (silt and clay content) for the samples that were not analytically processed. Prediction uncertainties were low with a Root Mean Square Error (*RMSE*) of 1.74 g/100 g for SOC (mineral soil), 3.84 g/100 g for SOC (peat soil), 0.05 g/100 g for total nitrogen (mineral soil), 0.19 g/100 g for total nitrogen (peat soil), 5.58 g/100 g for silt content and 1.31 g/100 g for clay content. The formula for *RMSE* is defined in section 2.8.1 below.

2.5. Soil organic carbon stock calculation

For those samples lacking bulk density information, multiple regression models were established using soil organic carbon content, soil type (mineral vs. peat), and sampling depth as input variables to predict soil bulk density (5-fold cross-validation, $R^2 = 0.91$, $RMSE = 0.1$ g/cm^3). In locations where the sampling depth was less than 1 m, we performed linear or exponential interpolation of SOC content and bulk density based on peat depth and soil type. The SOC stock (t/ha) of each sampling site within 1-meter depth was subsequently calculated using:

$$SOCstock = \sum_{i=1}^{n} SOC_i * BD_i * h_i \quad (1)$$

where, i indicates the i layer, n indicates the number of layers, SOC indicates soil organic carbon content (g/100 g), BD indicates soil bulk density (g/cm^3), and h indicates the thickness of each layer (cm).

2.6. UAV data acquisition

We carried out UAV flights with a DJI Matrice 300 RTK over the study area to collect high-resolution remote sensing data with four different sensors: (i) an Red-Green-Blue (RGB) camera (DJI Zenmuse P1 camera, 35 mm and 45 MP), (ii) a multispectral camera (MicaSense RedEdge-M camera with five discrete spectral bands: blue (475 nm), green (560 nm), red (668 nm), rededge (717 nm), and near infrared (842 nm), equipped with a downwelling light sensor), (iii) a LiDAR scanner (DJI Zenmuse L1, integrated with a 20-MP camera with a 1-inch CMOS sensor) and a thermal camera (TeAX thermal infrared camera, combined FLIR Tau2 cores and ThermalCapture hardware). The RGB and multispectral flights were conducted at above take-off point altitude of 90 m and a speed of 7.1 m/s. Both side and frontal overlap ratios were set to 80 %. In this case, the spatial resolutions of the RGB and multispectral images are approximately 6 cm and 12 cm, respectively. To enhance the LiDAR signal penetration, we chose the triple-echo mode with a sampling frequency of 160 kHz, maintaining a flight height of 50 m above the take-off point at a speed of 6 m/s. During the flight mission, the ground sampling distances varied between 1.16 cm and 2.18 cm per pixel. The IMU calibration procedures were conducted automatically at the beginning, during the mission, and after flight routes to ensure inertial navigation accuracy. The RGB and LiDAR flights were conducted in RTK positioning mode using a D-RTK 2 base station (DJI, Shenzhen, China). The base station was set up at a known point and was used to provide real-time positional corrections throughout the flight. For the multispectral camera, nine ground control points (GCPs) were used (50 cm × 50 cm targets). The GCPs were made of white laminated board stuck with aluminum foil in the diagonal area and were distributed across the study site during the flight mission. Their position was measured using an Emlid Reach RS2 GPS device, utilizing a post-processing RTK solution with the Belgian WALCORS network. One RGB and one LiDAR dataset were collected on 7th June 2023 and two multispectral datasets were collected on 19th April 2023 and 7th June 2023, respectively. Two thermal datasets (19th April 2023 and 4th July 2023) were used for land cover classification (see supplementary material).

2.7. UAV imagery processing

2.7.1. Image pre-processing

The multispectral images were processed with the Pix4D mapper software (Pix4D S.A., Lausanne, Switzerland) to generate orthophoto mosaics of the study area. Georeferenced reflectance maps of the five spectral bands were generated using the formula listed in Table 1 in RStudio V4.1.2 (*https://www.r-project.org/*). The RGB photos were processed in DJI Terra V4.0.10 (DJI, 2023) to generate an Ortho mosaic photo. The raw LiDAR data was pre-processed in the DJI Terra to provide a Digital Terrain Model (DTM;.tif file) with a resolution of 15 cm and a Digital Surface Model (DSM;.las file) (Wood, 1996). Subsequently, we conducted further processing of the LiDAR data in RStudio by the *lidR* package (*https://CRAN.R-project.org/package=lidR*). This involved the extraction of vegetation canopy height (CHM).

2.7.2. Wavelet transform

The wavelet transform was applied to derive DTM maps at various spatial scales. This approach, which allows undiscerned phenomena at different scales to be detected and enables multiscale analysis, has been widely used in high-resolution image processing such as

Table 1
Topographical and vegetation indices derived from LiDAR and multispectral images.

Index	Definition	Unit	Data source
RGB orthomosaic	Orthorectified image mosaicked from an RGB image collection	/	RGB
DSM	Digital Surface Model	m	LiDAR
DTM	Digital Terrain Model, the elevation	m	LiDAR
Slope angle	The rate of change of the elevation.	degree	LiDAR
TWI	Terrain wetness index: ln (As/tan(b)), where As is the specific contributing area and b is the slope angle in radians.	/	LiDAR
CHM	Canopy height model: DSM – DTM.	m	LiDAR
OSAVI2	Optimized Soil Adjusted Vegetation Index 2: 1.16*(*near infrared-red*)/(*near infrared* + *red* + 0.16)	/	Multispectral

geomorphological feature extraction (Lashermes et al., 2007), digital elevation model filtering (Kalbermatten et al., 2012), and soil surface noise removal (Aldana-Jague et al., 2016). Wavelet analysis is an extension of the windowed Fourier transform, which decomposes signals into shifted and scaled versions of a wavelet. The Haar wavelet is the simplest function and has been used for topography filtering (Bjorke and Nilsen, 2003). Besides the advantage of easy application, the two most important properties of the Haar wavelet are that it conserves the energy of the signals and performs a compaction of the energy of the signals (Walker, 2019). Therefore, most of the variance of the original data can be conserved after Haar's transform. Here, the original DTM was decomposed into eight levels using the wavelet toolbox in Matlab 2024a, with the Haar wavelet selected as the mother wavelet. During the decomposition process at each level, the image was divided into four sub-bands: the approximate image, which captures the low-frequency components, and three detail images that represent horizontal, vertical, and diagonal high-frequency components, respectively. For our study, we applied the inverse wavelet transform to reconstruct the image using only the approximate (low-frequency) sub-band from each decomposition level, thereby obtaining a version of the DTM that highlights its low-frequency features.

2.7.3. Environmental variables

Since each decomposition of the image reduced the number of pixels to half of the previous level, the reconstructed DTM maps at eight scales were thus resampled to the corresponding resolutions (0.30 m, 0.60 m, 1.20 m, 2.40 m, 4.80 m, 9.60 m, 19.2 m, 38.4 m) in ArcGIS 10.8. Slope angle (Wood, 2009) and terrain wetness index (TWI) (Böhner et al., 2001) at different scales were subsequently calculated by SAGA GIS 9.2.0. The Optimized Soil Adjusted Vegetation Index 2 (OSAVI2) (Henrich et al., 2009) was calculated in RStudio using the *raster* package (*https://cran.r-project.org/web/packages/raster/index.html*). Table 1 lists topographical and vegetation indices derived from RGB, multispectral, and LiDAR images.

2.8. Statistical analysis

All data analyses were then conducted in RStudio V4.1.2. To determine if there are significant differences among groups, the Analysis of variance (*ANOVA*) test was performed using the *stats package*. Pearson correlation analysis was conducted using the *corrplot package* (Murdoch and Chow, 1996). Multiple linear regression methods and Random Forest spatial mapping of peat thickness and SOC stock are introduced below.

2.8.1. Multiple linear regression models

Multiple linear regressions were performed using the *lm function* of the *stats package* (Wilkinson and Rogers, 1973), with peat thickness and SOC stock (top 1 m) as responses. The regression models were defined as:

$$Response = \sum_{j=1}^{x} \beta_j * X_j + \beta_0 \quad (2)$$

where, X indicates the independent variable, j indicates the j^{th} variable, x indicates the number of variables, β indicates the coefficient of the variable, and β_0 indicates the intercept. The independent variables considered for peat thickness were the topographic variables and vegetation indices as listed in Table 1, while peat thickness, topography, and vegetation were selected for SOC stock. Estimates for these variables were extracted from the UAV-derived maps by retrieving the value of the in-situ observation points for peat thickness or SOC stock. Independent variable coefficients, coefficient of determination (R^2), and modelled peat thickness or SOC stock values were extracted using the *summary function* after running each model. The relative importance of each variable was subsequently obtained using the *relaimpo* package. To assess multicollinearity in regression analysis, the *car package* was used to calculate the variance inflation factor (*VIF*) (Fox and Monette, 1992). In addition, we calculated the Akaike Information Criterion corrected for small sample sizes (*AICc*) of all models using the *AICcmodavg package 2.3-2* (MacKenzie et al., 2002), which can create model selection tables. The Root Mean Square Error (*RMSE*) was also used to assess the quality of the regression model fit:

$$RMSE = \sqrt{\frac{1}{m}\sum_{k=1}^{m}(obs_k - pred_k)^2} \quad (3)$$

where m is the sample size and k indicates the k^{th} sample. The *obs* and *pred* are vectors of observed and predicted values, respectively.

2.8.2. Random Forest spatial models

In addition, we used Random Forest techniques (Breiman, 2001) to spatially map peat thickness and carbon storage by considering different sources of datasets (i.e., topography, vegetation, and peat thickness) independently and in combination, to compare with the multiple linear modeling (stated in the MLR section 2.8.1). Firstly, we separated the dataset into a training sample (70 %) and a testing sample (30 %) using K-means clustering as this method could avoid biases that might occur with random sampling (Hair et al., 2010). Specifically, the dataset was converted to a matrix and then we performed Principal Component Analysis (PCA) to reduce dimensionality while retaining 99.9 % of the variance. After that, K-means clustering was applied to the PCA scores to cluster data into groups by performing 10,000 iterations. We then selected 70 % of the data points for the training set by choosing representative samples from the center of each cluster and the remaining 30 % were used as the test set. Secondly, we trained the models by the 5-fold cross-validation method (Mosteller and Tukey, 1968) and subsequently validated the model accuracy with the test dataset. The *RMSE* and R^2 were also used to assess the quality of the random forest model fit. Finally, we made predictions of peat thickness and carbon stock (top 1 m) for the study area.

In a recent review, Minasny et al. (2019) pointed out that one of the notable gaps in current peat mapping is that only 19 % of studies have quantified uncertainty in maps. In our study, the techniques employed for uncertainty analysis were based on the methodologies described in Zhou et al. (2022) and Malone et al. (2011). Firstly, each set of training samples was subject to 100 bootstraps to stabilize the prediction model performance and to calculate the variance of the prediction. Hence, 100 models were created, resulting in 100 prediction maps of the area. The

mean value of the 100 maps were calculated as the final prediction map. The variance (VAR_{boot}) of the 100 predictions and the mean squared error from the testing data (MSE_{vali}) were used to quantify the uncertainty for each pixel. Subsequently, we calculated an overall prediction accuracy (VAR_{all}) for all pixels of the study area, which is the sum of VAR_{boot} and MSE_{vali}. The prediction interval range was calculated by:

$$PIR = 2^{*}\sqrt{VAR_{all}}^{*}Z \quad (4)$$

where *PIR* indicates the prediction interval range and *Z* indicates the z-score value that corresponds to the 90 % probability (*Z*=1.64). Finally, the relative uncertainty of the peat thickness and SOC stock estimates was expressed as ±half of the PIR as a percentage of the mean prediction.

$$Uncertainty = 0.5^{*}PIR/Meanpred \quad (5)$$

where *Uncertainty* indicates the relative uncertainty of predictions and *Meanpred* indicates the mean value of the 100 prediction maps.

3. Results

3.1. Exploratory data analysis

3.1.1. Soil bulk density and SOC content

In our study case, peat soil is defined as soil with an SOM content ≥30 % according to the digital soil map of Southern Belgium (Veron et al., 2005) and Joosten and Clarke (2002). Fig. 2 presents soil bulk density and SOC content of both peat and mineral soil samples. As expected, the bulk density of mineral soil was significantly greater than that of peat soil (*ANOVA*, $p < 0.05$), with mean values (±standard deviation (SD)) of 1.06 g/cm^3 (±0.35 g/cm^3) and 0.22 g/cm^3 (±0.11 g/cm^3), respectively (Fig. 2a). Soil bulk density increases significantly with soil depth (*ANOVA*, $p < 0.05$), from 0.26 g/cm^3 (±0.17 g/cm^3) in the top 20 cm to 0.40 g/cm^3 (±0.35 g/cm^3) in the ~20–40 cm soil, and then to 0.85 g/cm^3 (±0.53 g/cm^3) in the subsoil (Fig. 2c). Peat soils are rich in organic carbon as illustrated in Fig. 2b and Fig. 2d, with an average SOC content of 37.47 g/100 g (±7.26 g/100 g), which was around 8 times greater than that found in mineral soils (4.55 ± 4.02 g/100 g). The vertical distribution of SOC content showed an opposite pattern to that of bulk density, with SOC content decreasing from 35.25 g/100 g (±9.80 g/100 g) in the top 20 cm to 28.75 g/100 g (±16.13 g/100 g) in the ~20–40 cm soil, and then to 14.43 g/100 g (±16.77 g/100 g) in the ~40–60 cm (Fig. 2d). Other soil properties including SOM content, clay content, and silt content can be found in Table S2 of the appendix.

3.1.2. Peat soil thickness

Fig. 3 shows the peat horizon thickness along the middle transect as derived from the GPR data (Henrion et al., 2024). We used a GSSI GPR system (Geophysical Survey Systems, Inc., Nashua, NH, USA) with a 200-MHz center frequency antenna. The system was operated on-ground to provide detailed subsurface images down to depths of more than 2 m. From the top of the hill to the floodplain, peat soil thickness widely varied at small scales, ranging from 0.2 m to 2.1 m. Statistical results of both GPR-derived and soil-sampling-derived peat thickness (Fig. 4a) indicate that peat thickness in the foot slope area was significantly greater (1.04 ± 0.55 m) than that in any other slope positions (*ANOVA*, $p < 0.05$), followed by the shoulder (0.63 ± 0.28 m), the summit (0.61 ± 0.18 m), and the backslope (0.60 ± 0.23 m). The shallowest peat layer was found on the top slope of the hill and floodplain, with an average value of 0.37 ± 0.20 m and 0.36 ± 0.14 m, respectively. By performing a comparison among different vegetation types (Fig. 4b), we found that the peat horizon under dwarf shrub vegetation was the thickest with a value of 0.70 ± 0.41 m, followed by *Molinia caerulea* (0.62 ± 0.41 m), which, however, was not significantly deeper than the other two types (*Juncus acutus* 0.52 ± 0.25 m, and trees 0.55 ± 0.24 m) (*ANOVA*, $p < 0.05$).

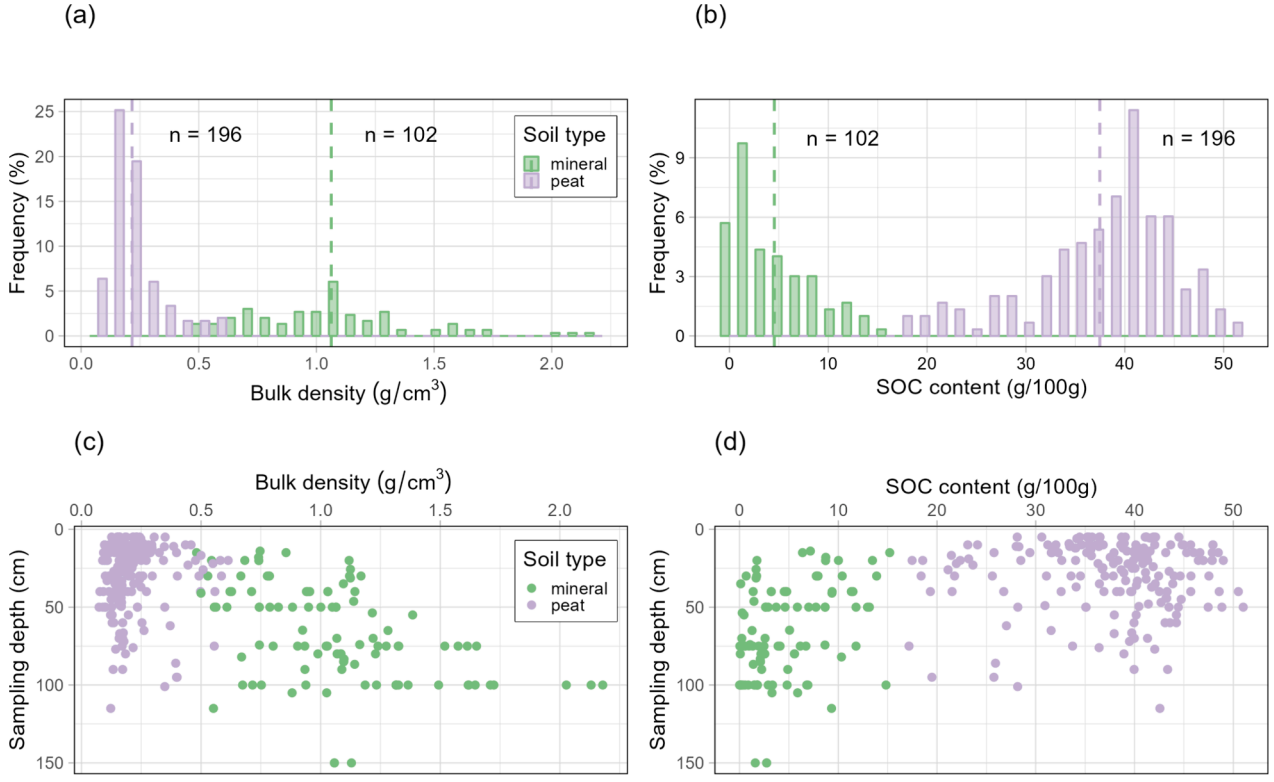

Fig. 2. Histogram and depth distribution of soil bulk density (a and c) and SOC content (b and d) from soil sampling. The colour indicates different soil types (mineral or peat soil). The dashed line indicates the mean value and *n* indicates the number of *in situ* observations.

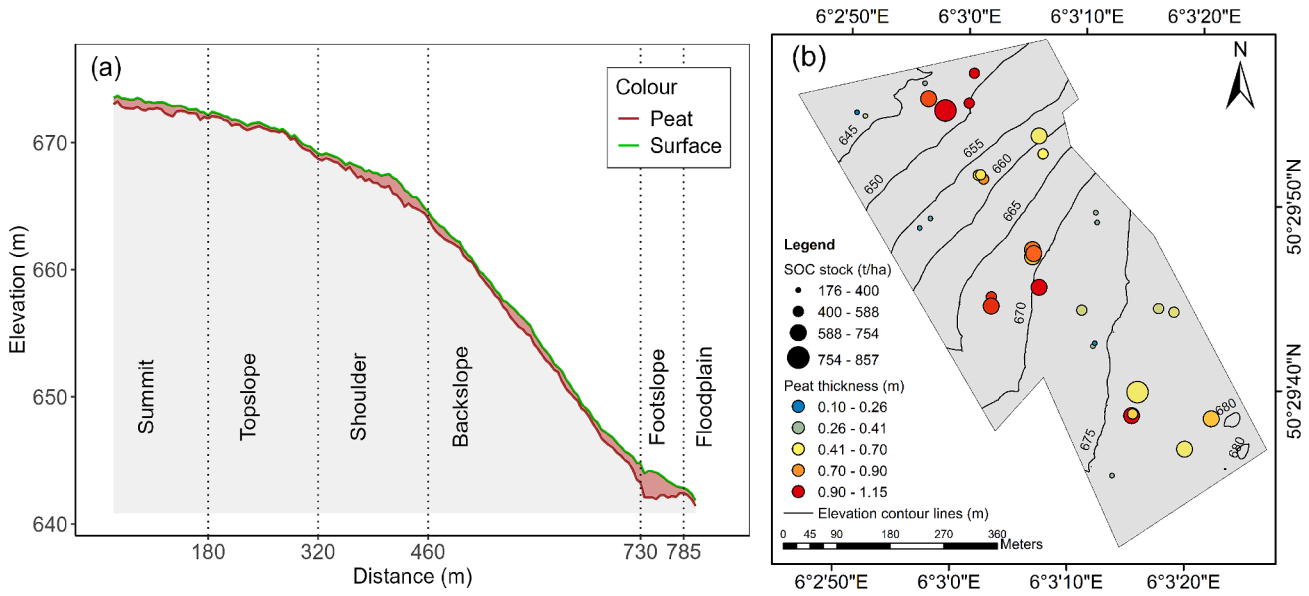

Fig. 3. The GPR-derived peat horizon and UAV LiDAR-derived elevation along the middle transect (a), modified from Henrion et al. (2024). Slope positions were classified by elevation: Floodplain (elevation < 643 m), Footslope (643 m ≤ elevation < 650 m), Backslope (650 m ≤ elevation < 660 m), Shoulder (660 m ≤ elevation < 670 m), Topslope (670 m ≤ elevation < 673 m), Summit (elevation ≥ 673 m). The brown colour indicates the peat horizon. Figure (b), the spatial distribution of SOC stock and peat thickness with 10 m elevation contour lines in black colour. The colour of the circle indicates peat thickness, and the size indicates the magnitude of the carbon stock.

3.1.3. SOC stock

As shown in Fig. 3 and Fig. 4c, SOC stock for the 1 m soil profile was highly heterogeneous across the landscape, ranging from 176.13 t/ha to 856.57 t/ha. Overall, the SOC stock at the top slope area (375.17 ± 83.41 t/ha) and floodplain (371.93 ± 41.81 t/ha) were significantly lower compared to the summit and shoulder positions in the hillslope-floodplain system (*ANOVA*, $p < 0.05$). Abundant carbon was observed at the shoulder and summit of the hill, with an average storage of 671.71 ± 55.66 t/ha and 615.83 ± 149.45 t/ha, respectively. There was no significant difference between the backslope (469.13 ± 150.15 t/ha) and the footslope (604.28 ± 148.48 t/ha) (*ANOVA*, $p < 0.05$). In the vertical direction, SOC stock at the soil surface was significantly larger than that of subsoil (*ANOVA*, $p < 0.05$), except for at the shoulder and summit (Fig. 4e). The carbon storage under different vegetation types also exhibited heterogeneity (Fig. 4d), with trees (664.45 ± 126.56 t/ha) having the highest mean SOC stocks, followed by dwarf shrubs (563.22 ± 124.177 t/ha), *Juncus acutus* (477.87 ± 189.91 t/ha), and *Molinia caerulea* (535.32 ± 176.66 t/ha). Additionally, Fig. 4f indicated that carbon stocks in soils under trees do not vary significantly with depth, while carbon stocks under other vegetation cover types decrease with depth (*ANOVA*, $p < 0.05$).

3.2. Factors contributing to spatial variability in peat thickness and SOC stock

3.2.1. Micro vs macro-scales

To quantify the contribution of environmental factors to the spatial heterogeneity of peat thickness and carbon stocks, multiple linear regressions were performed using topographic variables (i.e., elevation, slope, TWI), vegetation height (CHM), and vegetation index OSAVI2 as input variables. At the original scale (resolution: 0.15 m), topographic and vegetation factors explained 27 % of the spatial variability in peat thickness (Fig. 5a), while these factors combined with peat thickness explained 64 % of the spatial heterogeneity in carbon stocks (Fig. 5b). To explore the impact of variation in topographic scale on the regression models' explanatory power, wavelet transform was utilized to derive topographic variables at different scales (Fig. 5c-5e present examples for TWI). As illustrated by Fig. 5f, the peat thickness prediction performance improved at larger scales, with R^2 increasing from 0.27 to 0.47 to level 6, and then decreasing at level 7 and level 8. However, the SOC storage model performs better at the fine scales, with the model's R^2 decreasing and RMSE increasing with larger scales (Fig. 5g).

3.2.2. Relative contribution of environmental factors at relevant scales

Fig. 5f and g illustrate that the optimal topographic scale for the peat thickness regression model is level 6, whereas for the carbon stock regression model it is level 2. Hence, we quantified the relative contribution of environmental factors by considering the relevant topographic scales. As shown in Table 2, topography alone can explain 46 % of the observed variance in peat thickness. Vegetation factors (CHM and OSAVI2) have a prediction power of 3 %, whereas combining both types of variables did not improve the model explanation capacity, with topography and vegetation accounting for 44.5 % and 2.5 %, respectively. In addition, the *AICc* increased slightly by the presence of vegetation variables (Table 2), which further suggests that the current vegetation distribution does not explain the spatial distribution of peat thickness.

Multiple linear regressions were also performed to identify controlling factors for SOC stock. The regression analysis of peat thickness and topographic attributes with carbon storage (Table 2) showed that they had a prediction power of 46 % and 21 %, respectively. The contribution from vegetation was limited, at only 16 %. When all environmental factors were taken into account, the regression model yielded the best explanation capacity of carbon stock variance ($R^2 = 0.64$), although the *AICc* increased slightly due to the inclusion of vegetation.

3.3. Mapping using UAV data

3.3.1. Peat thickness maps

The peat thickness spatial model, based on the random forest algorithm and UAV-derived input variables, showed robust performance in both scenario 1 (i.e., considering only topographic variables: elevation, TWI, and slope) and scenario 3 (i.e., considering both topographic (elevation, TWI, and slope) and vegetation variables (CHM and OSAVI2)) (Table 3). In contrast, the model performance was poor when only the vegetation factors were considered (scenario 2). The R^2 values

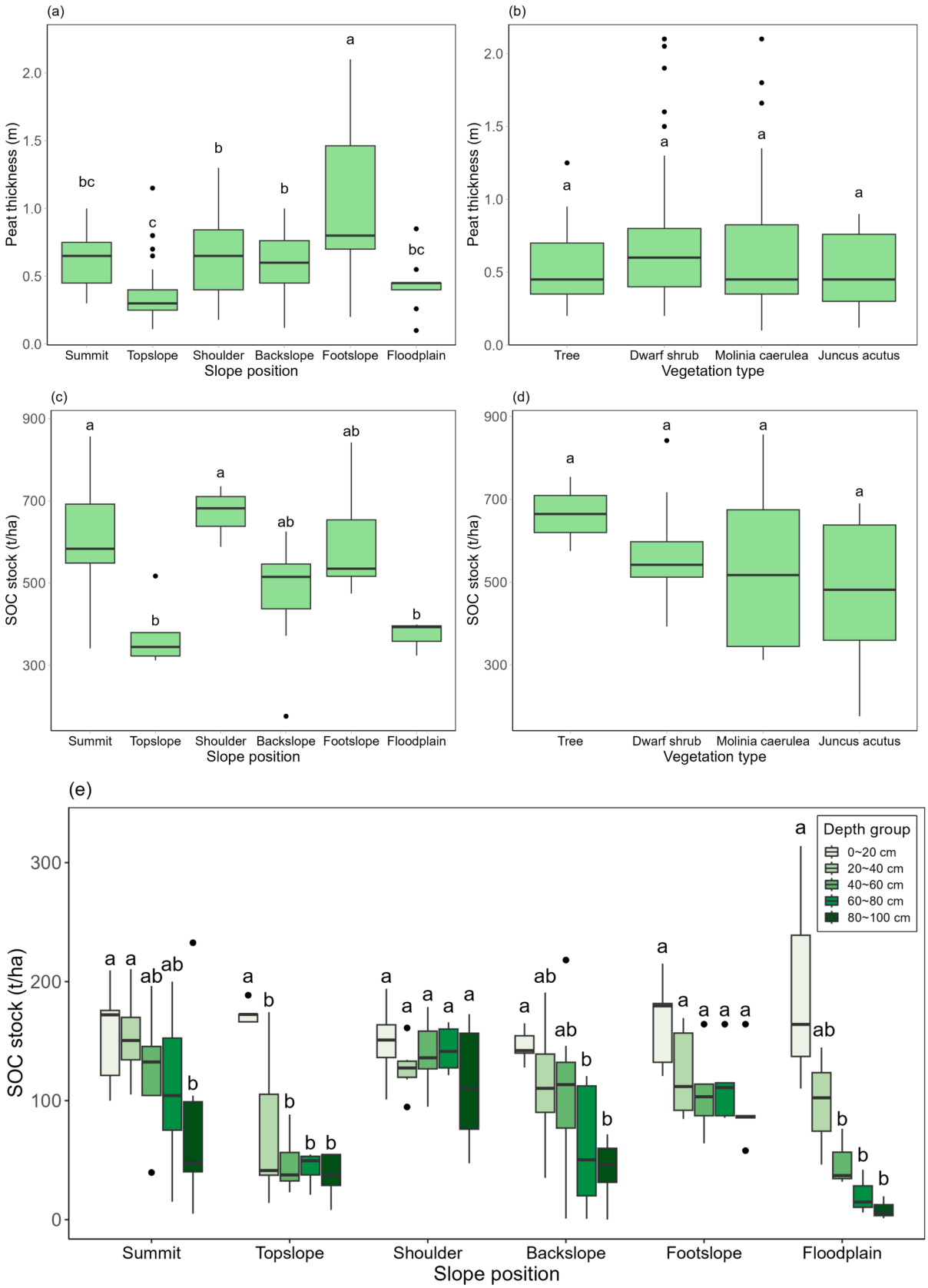

Fig. 4. The peat thickness ($n = 190$) and SOC stock (top 1 m, $n = 35$) of different slope positions (a) (c) and different vegetation types (b) (d). Figures e-f illustrate the depth distribution of SOC stock within five soil depth intervals (0 ~ 20 cm, 20 ~ 40 cm, 40 ~ 60 cm, 60 ~ 80 cm, and 80 ~ 100 cm) across different slope positions and vegetation types, respectively. The box edges represent the first quartile (Q1) and the third quartile (Q3), and the line inside the box shows the median. Whiskers extend from the box to the smallest and largest values within 1.5 times the interquartile range. Points outside the whiskers are considered outliers. The *ANOVA* tests were conducted within each class with boxes of the same letters indicating no significant difference in the peat thickness or SOC stock.

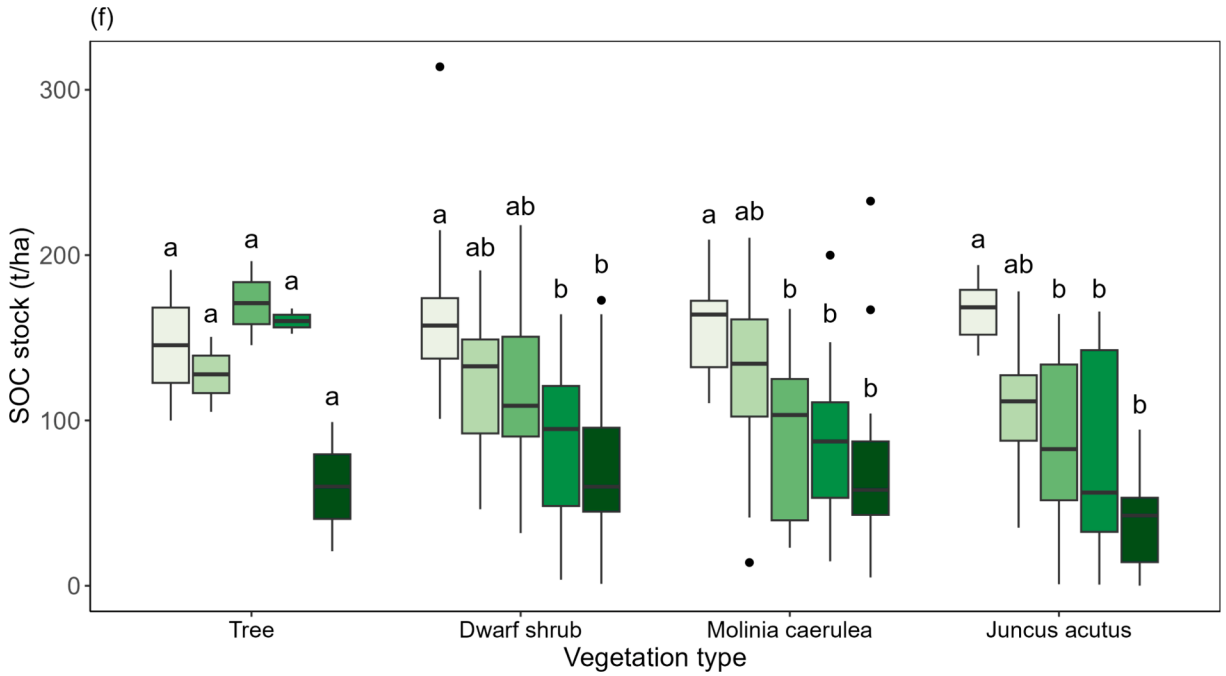

Fig. 4. (*continued*).

were 0.94 and 0.88 for the training dataset and the test dataset, respectively, when considering only topographic variables. In the third scenario, the high R^2 (0.94 and 0.85) and relatively small *RMSE* values (0.09 m and 0.16 m) on both datasets implied that the model was well-fitted.

The predicted peat thicknesses range from 0.27 m to 1.67 m (Fig. 6a), with a mean ± SD value of 0.65 ± 0.22 m, which is relatively similar to the range of values observed (range: 0.1–2.1 m, mean ± SD: 0.62 ± 0.37 m). The deepest peat layer was located at the foot of the slope, especially at elevations between 644 and 645 m, with an average peat thickness of around 0.88 ± 0.25 m. Another thick peat horizon was found on the shoulder of the hill, located at elevations between 666 and 668 m, with an average thickness of about 0.85 ± 0.14 m. Peat thickness predicted at the backslope were subsequently deeper (0.65 ± 0.12 m), which were consistent with our measurements (0.60 ± 0.23 m). The predicted peat soil thickness at the summit (0.50 ± 0.31 m) were shallower than the depth measured by auger and GPR (0.56 ± 0.06 m), while the estimated thickness at the topslope (0.47 ± 0.13 m) was higher than our measurements (0.37 ± 0.20 m). In addition, the peat thickness at the floodplain (0.84 ± 0.34 m) were overestimated compared to our measurements (0.36 ± 0.14 m), with values ranging from 0.34 m to 1.56 m. Large relative prediction uncertainty occurs in the topslope and summit areas, as shown in Fig. 6b.

3.3.2. SOC stock maps

The Random Forest model used for predicting SOC stock also showed good performance metrics. When using terrain attributes (elevation, slope, TWI) and vegetation (CHM and OSAVI2) as predictors separately, the high R^2 values on the training set indicated a strong agreement between observed and predicted SOC stock (Table 3). However, on the test set, the R^2 below 0.48, the larger *RMSE* (110.17–163.94 t/ha) suggests a reduced predictive performance, potentially due to the model's challenges in extrapolation to sites with other environmental characteristics. This situation improved significantly when three types of factors (i.e., peat depth, elevation, slope, TWI, CHM, OSAVI2) are considered simultaneously (R^2 = 0.85, *RMSE*=59.25 t/ha).

The predicted SOC stock map shows great heterogeneity (Fig. 6c). As revealed in the map, higher carbon storage was observed at the summit with an average value ± SD of 609.60 ± 23.20 t/ha. A large SOC stock is also found in the shoulder, with a mean estimated stock of 596.58 ± 30.13 t/ha. In contrast, less SOC is stored at the floodplain (570.67 ± 26.92 t/ha) and the backslope positions (568.47 ± 26.28 t/ha), while both predictions overestimated the SOC stock when compared with the measurements. In particular, the predicted SOC stock in the floodplain is ~200 t/ha higher than the observations. Overall, the mean predicted SOC stock (590.22 ± 32.85 t/ha) across the landscape is close to our field measurements (539.14 ± 160.98 t/ha). Although large uncertainties could be seen in the floodplain and topslope, most of the relative uncertainties were less than 30 % (Fig. 6d), suggesting that the carbon stock estimates were robust.

4. Discussion

4.1. Peat thickness across the landscape

4.1.1. Spatial variability of peat thickness and its associated environmental factors

Peat thickness shows great variability across the landscape, with thicker peat deposits occurring on flatter areas such as the footslope of the hill and shallower peat developing at the topslope area (Fig. 3 & Fig. 4a). Consistent with other studies, our findings indicate that topography plays a critical role in shaping peat thickness (Cobb et al., 2024; Holden and Connolly, 2011; Illés et al., 2019; Parry et al., 2014; Rudiyanto et al., 2018). However, the contribution from surface topography varies with scale, with macro-topography explaining more of the variation in peat thickness than micro-topography (Fig. 5f). This is likely because peat is formed over thousands of years on pre-existing landscapes (Frankard et al., 1998), whereas the evolution of the micro-topography of peat surfaces is more influenced by recent biogeomorphological processes and human activities operating at much shorter timescales (Li et al., 2018). Additionally, peat accumulation is highly correlated with spatial patterns in soil hydrology (Minasny et al., 2023), which are controlled by processes operating at the macro scale, as opposed to micro scale processes such as microbial activity and temperature.

When considering the respective relevant scales for the 3 terrain attributes— i.e., elevation, slope and TWI—, ca. 46 % of peat thickness variance was explained, whereas the inclusion of vegetation did not

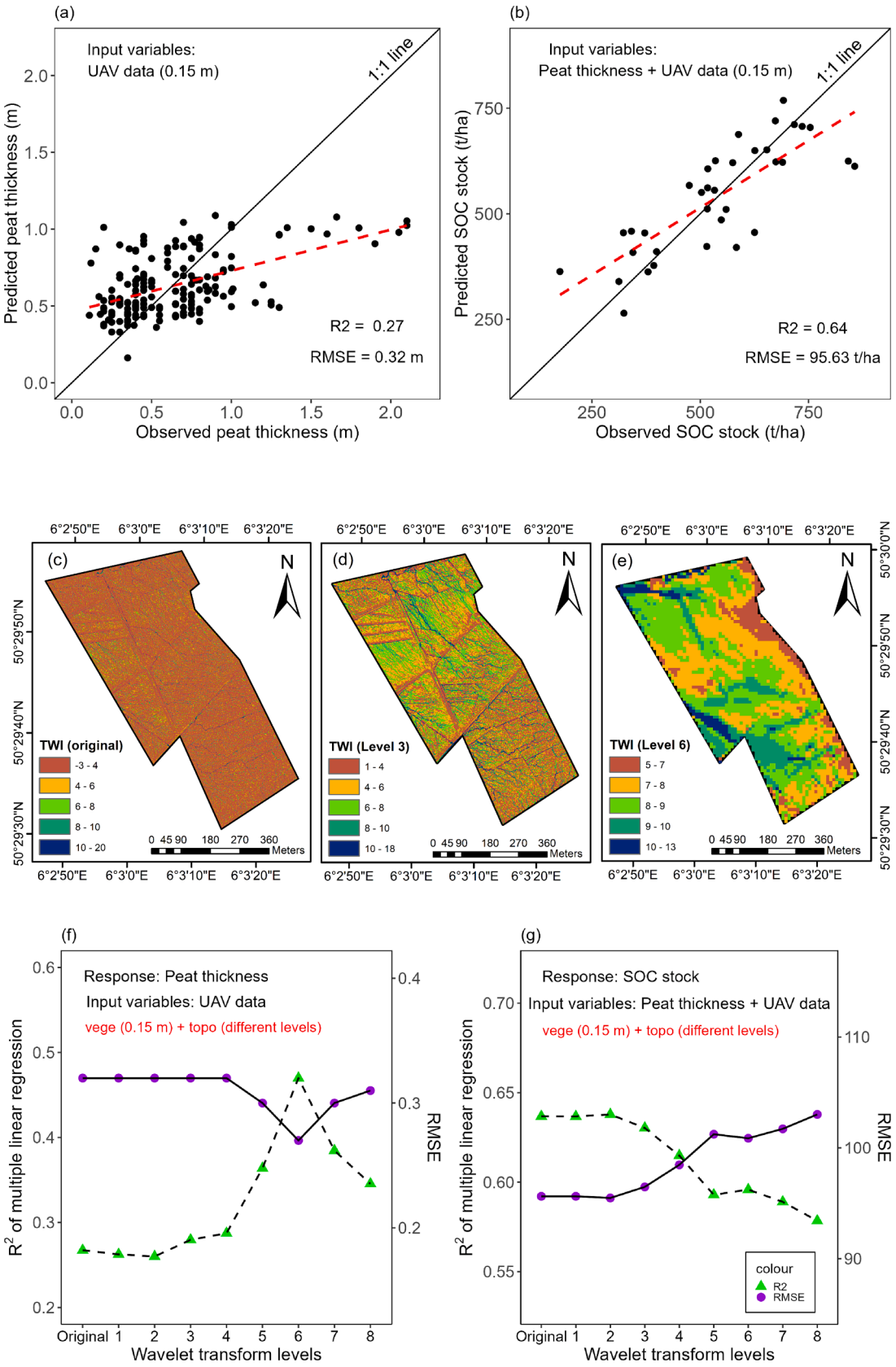

Fig. 5. Figures a-b show the observed versus predicted peat thickness (a) and SOC stock (b) at the original scale (resolution: 0.15 m) by performing multiple linear regression. Figures c-e show examples of terrain wetness index (TWI) at different wavelet transform scales: original (c), level 3 (d), level 6 (e). Figures f–g show the impact of topography from the original scale to level 8. The colour and shape indicate R^2 and *RMSE* of the multiple linear regression models at different wavelet transform levels.

Table 2
Coefficients and relative contributions of input variables (peat thickness, elevation, TWI, slope, CHM, OSAVI2) of multiple linear regression models for predicting peat thickness and SOC stock of the top 1 m. The *Topo.* indicates that the input variables include elevation, TWI, and slope. The *Vege.* indicates that the input variables include CHM and OSAVI2. The *Topo.* + *Vege.* indicates that the input variables include both topographic and vegetation variables. Model performance was evaluated by *AICc*, R^2, and *RMSE*.

Models		Response: Peat thickness			Response: SOC stock				
		Topo.	*Vege.*	*Topo.* + *Vege.*	Peat thickness	*Topo.*	*Vege.*	*Topo.* + *Vege.*	Peat thickness + *Topo.* + *Vege.*
Input variables: coefficient (contribution)	Peat thickness	/	/	/	326.04*** (46 %)	/	/	/	289.54*** (39 %)
	Elevation	−0.02*** (23 %)	/	−0.02*** (21 %)	/	1.68 (3 %)	/	2.08 (3 %)	3.02 (5 %)
	TWI	0.23*** (19 %)	/	0.25*** (19 %)	/	−25.07* (12 %)	/	−22.72* (11 %)	−15.98 (8 %)
	Slope	−0.02 (5 %)	/	−0.02 (5 %)	/	−20.08 (6 %)	/	−15.53 (5 %)	−13.40 (4 %)
	CHM	/	−0.02 (0.07 %)	−0.06 (0.5 %)	/	/	64.20 (5 %)	26.18 (2 %)	0.48 (1 %)
	OSAVI2	/	−0.46 (3 %)	−0.14 (1 %)	/	/	−473.01* (11 %)	−433.72* (11 %)	−228.85 (7 %)
Model performance	Intercept	13.05***	0.92***	12.08***	354.17***	−364.95	802.54***	−413.26	−1352.59
	AICc	58.09	163.07	60.33	438.89	457.64	457.33	458.78	439.99
	R^2	0.46	0.03	0.47	0.46	0.21	0.16	0.32	0.64
	RMSE	0.28	0.37	0.27	116.07	140.67	145.63	131.07	95.48

Significance level: *** P < 80.001, ** P < 0.01, * P < 0.05.

Table 3
Random Forest model performance for peat thickness and SOC stock (top 1 m) spatial mapping. The numbers in parentheses in the first column on the left indicate the sample sizes of training and testing datasets. The *Topo.* indicates that the input variables include elevation, TWI, and slope. The *Vege.* indicates that the input variables include CHM and OSAVI2. The *Topo.* + *Vege.* indicates that the input variables include both topography and vegetation variables.

Response	Input variables	Training dataset		Testing dataset	
		RMSE	R^2	*RMSE*	R^2
Peat thickness (133, 57)	*Topo.*	0.09	0.94	0.14	0.88
	Vege.	0.20	0.74	0.34	0.03
	Topo. + *Vege.*	0.09	0.94	0.16	0.85
SOC stock (24, 11)	Peat thickness	69.79	0.81	74.47	0.76
	Topo.	84.23	0.73	110.17	0.48
	Vege.	84.20	0.69	163.94	0.10
	Peat thickness + *Topo.*	60.11	0.86	59.75	0.85
	Peat thickness + *Topo.* + *Vege.*	51.76	0.90	59.25	0.85

significantly improve the model prediction capacity (Table 2). Elevation was the most important factor in controlling the spatial distribution of peat thickness (Table 2). This may be because large amounts of partly decomposed plant debris first filled depressions or flat ground and then expanded laterally (Wastiaux et al., 2000). As a result, thicker peat is observed in the footslope, shoulder, and summit areas (Fig. 4a). The shallow peat depth in the floodplain can be attributed to the influence of colluvial or alluvial deposits originating from the Polleur River (Houbrechts et al., 2018). However, the contribution from elevation (around 23 %) was less than that found in previous studies (e.g., Vernimmen et al. (2020) (83 ~88 %); Rudiyanto et al. (2016b) (variable usage: 79.7 ± 6.9 %)), implying peat distribution might be affected by other terrain attributes, hydrological conditions, or human impacts (e.g., drainage and past vegetation) along the elevational gradient.

Parry et al. (2012) suggested that models using only slope and elevation as input parameters could account for more than 50 % of the variance of peat thickness. This is because the slope imposes an important control on water movement and retention, and thereby on peat erosion and deposition (Graniero and Price, 1999). However, unlike Gatis et al. (2019), who identified slope as a more influential predictor than elevation, our study found a weak relationship between slope and peat thickness (Table 2). Terrain wetness index (TWI)—a measurement that considers both the drainage basin on the downslope and the water contribution from the upslope (Moore et al., 1993)—exhibited a positive correlation with peat soil thickness in our study case (Table 2), likely because waterlogged conditions create ideal environments for peat accumulation. However, it should be noted that numerous ditches have been dug in the study area for drainage in the last century, which may have altered the original hydrologic patterns and accelerated peat erosion and peat *in situ* subsidence (Holden et al., 2004), weakening the linkage between surface conditions and peat thickness.

Vegetation attributes can be an indicator of waterlogged conditions and peatland status (Beyer et al., 2021; Harris et al., 2015; Palozzi and Lindo, 2017; Sutton-Grier and Megonigal, 2011). However, our regression analysis implied that current vegetation could only explain around 3 % of peat thickness variability (Table 2). Gatis et al. (2019) demonstrated that land management at the margin of peatlands has led to changes in vegetation cover, disrupting the connection between the vegetation and the underlying peat. In our study area, anthropogenic disturbances such as drainage, spruce planting, and logging have altered the vegetation type, which in turn affects its correlation with peat.

Approximately 53 % of the variability in peat thickness remained unexplained by the multiple linear regression, suggesting peat soil thickness may be influenced by other factors such as subsurface topography or variations in the lithology of the parent material and associated variations in deep drainage. Soil coring surveys (Henrion et al., 2024) showed the presence of a grey clay-rich horizon beneath the peat soil, whereas a yellow silt horizon with rock fragments can be seen at the top slope of the hill. This silty soil horizon is characterized by better drainage conditions compared to clay-rich horizons, which may explain the shallower peat thickness on the top slope.

4.1.2. Peat thickness mapping and uncertainties

Previous studies have shown that peat thickness can be mapped using only surface topographic covariates (Parry et al., 2012; Rudiyanto et al., 2015) or with the additional consideration of other environmental

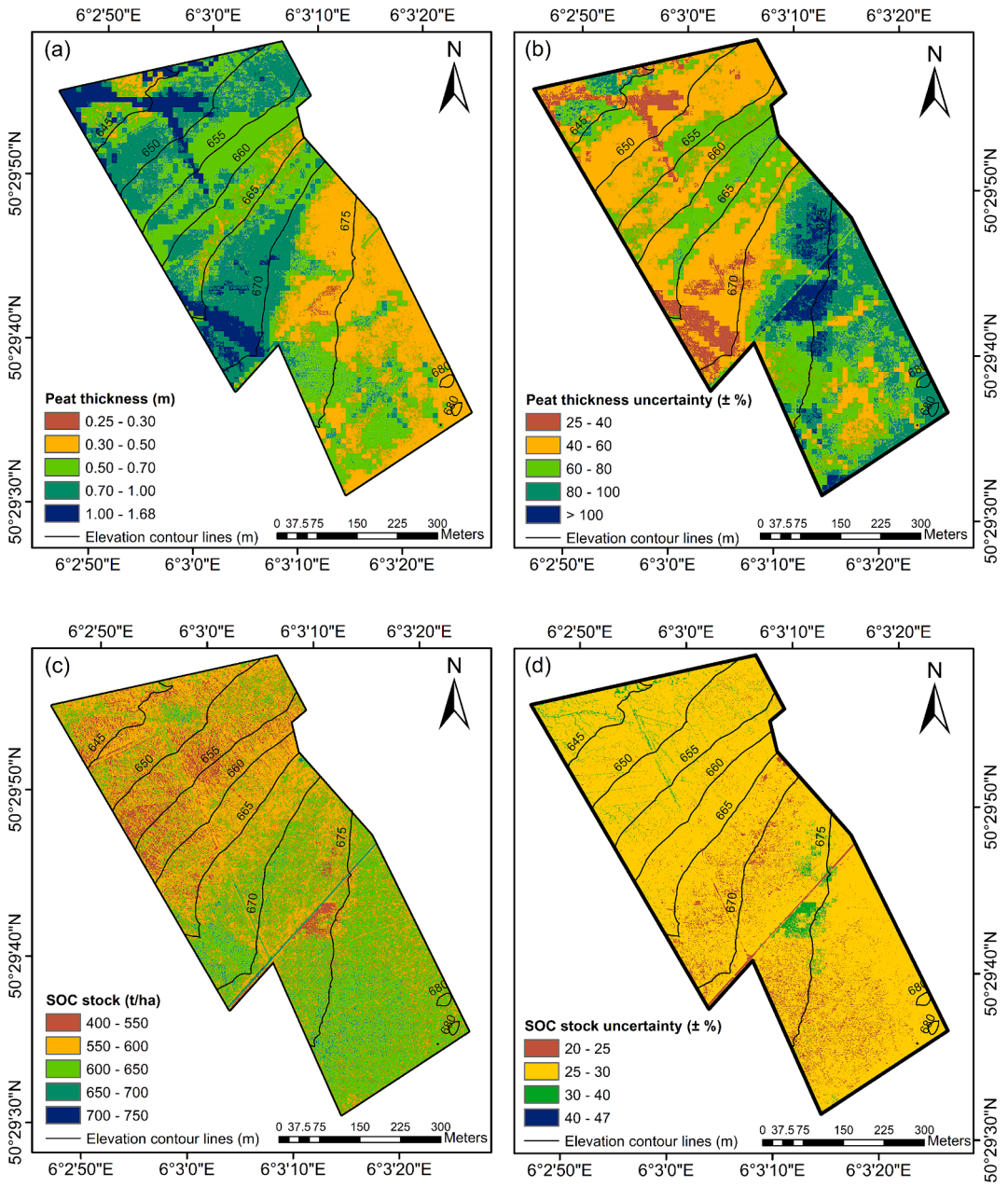

Fig. 6. Maps of predicted peat thickness, SOC stock, and relative uncertainty across the landscape. Figure (a), mean prediction of peat thickness (m) from 100 random forest models with five predictors: elevation (level 6), TWI (level 6), slope (level 6), CHM (original scale), and OSAVI2 (original scale). Figure (b), relative uncertainty of peat thickness prediction, expressed as ± half of the prediction interval range as percentage of the mean prediction. Figure (c), mean prediction of SOC stock (t/ha) of top 1 m from 100 random forest models with six predictors: mean prediction of peat thickness, elevation (level 2), TWI (level 2), slope (level 2), CHM (original scale), and OSAVI2 (original scale). Figure (d), relative uncertainty of SOC stock prediction, expressed as ± half of the prediction interval range as percentage of the mean prediction. The black lines on all maps indicate elevation contour lines (m).

variables, such as vegetation and soil type (Young et al., 2018), the distance to the river (Rudiyanto et al., 2016b), radiometric dose (Gatis et al., 2019; Koganti et al., 2023), and disturbance (Holden and Connolly, 2011). Here, we demonstrated that peat thickness across a hillslope-floodplain transition is affected by various types of environmental factors. However, the multiple linear regression models achieved only a modest fit (R^2 = 0.47, *RMSE* = 0.27 m), similar to the model performance of Young et al. (2018). Given the heterogeneous nature of the landscape, we therefore developed a Random Forest spatial model to estimate peat thickness. The tree-based model is capable of capturing complex nonlinear relationships and has proved to be more suitable for depicting the intricate interactions between environmental factors and peat thickness (Rudiyanto et al., 2016b; Rudiyanto et al., 2018).

We found that the Random Forest spatial model with only three terrain variables performed very well in the testing dataset (R^2 = 0.88, *RMSE* = 0.14 m), outperforming Parry et al. (2012) who mapped peat thickness based on a functional relationship with elevation and slope derived from airborne radar data. Theoretically, using data from different sources could improve peat thickness mapping accuracy, as they provide information on different aspects of peatland structure and function (Minasny et al., 2023). However, our study found that the inclusion of vegetation decreased the predictive power by 3 % (Table 3), suggesting the limited contribution of the multispectral sensor in our study. Overall, our approach yielded a more robust estimation compared to those studies that utilized airborne LiDAR data (e.g., Gatis et al. (2019) (R^2 = 0.55–0.66, *RMSE* = 0.31–0.35 m)), or that were based on

coarse satellite images (e.g., Fiantis et al. (2023) (R^2 = 0.44, *RMSE* = 1.41 m), Rudiyanto et al. (2018) (R^2 = 0.5–0.7, *RMSE* = 1.8–2.8 m)). This might be explained by the utilization of UAV-LiDAR, which enables the characterization of heterogeneous landscapes above the surface with very high spatial resolution. Additionally, the application of wavelet transform allows us to identify the relevant scale to analyze relationships between peat thickness and topographical features.

However, interpreting peat thickness only from surface conditions may bring uncertainties (Silvestri et al., 2019b). Direct information on peat thickness derived from airborne gamma-ray data from the radioactive decay of K, U, and Th in the underlying mineral soil has been proven to be useful in optimizing peat thickness mapping (Gatis et al., 2019; Keaney et al., 2013). However, because gamma radiation is severely attenuated when peat soil thickness is greater than 0.6 m, greater peat depths are difficult to resolve (Gatis et al., 2019). Also, preprocessing of the raw UAV data (i.e., georeferencing, wavelet transform, resampling) to produce the topography and vegetation variables may have introduced errors in the model. In addition, our sampling strategies for peat thickness modelling may be another source of uncertainty. The training and testing data was from a mixed dataset obtained by both GPR and manual probing approaches. Peat thickness in 42 sites of three transects were determined by augering, but it should be noted that more sampling sites were in the middle transect (Fig. 1a). A dataset of 148 samples resulting from the GPR survey was collected at the middle transect as well. Consequently, we have fewer samples distributed on the edges of the peatlands, thereby generating higher uncertainties in these places. To obtain a better representation, the transect cross clusters sampling approach proposed by Rudiyanto et al. (2016b) could be considered. Larger uncertainty occurs at the topslope and summit (Fig. 6b), implying that other factors besides surface topography and vegetation control peat development in this area. The results emphasize that factors such as water table depth, permeability of the underlying deposits or bedrock, and peat bottom morphology play a role in the formation and storage of peat in these areas.

4.2. SOC storage across the landscape

4.2.1. Spatial variability of SOC storage and its associated environmental factors

Our field measurements indicate that around 539.14 ± 160.98 t/ha organic carbon is stored within the top 1 m profile across the landscape, which is approximately 5.33 times higher than the mean carbon stored in aboveground live tree biomass of Belgian forests (~101 t/ha) (Walle et al., 2005), 3.65 times higher than grasslands (~147.7 t/ha) (Mestdagh et al., 2009), and 6.45 times higher than croplands (~83.64 t/ha) (Sleutel et al., 2003). We also observe that the carbon stock is spatially organized, showing considerable variability in both horizontal and vertical directions (Fig. 3 & Fig. 4). Although peat thickness could explain more variance of SOC stock in the MLR analysis (Table 2), here we do not discuss its contribution considering the fact that SOC content of peat soil is significantly higher than that of mineral soil (Fig. 2b).

The predictive ability of topographic metrics varies from micro to macro scales (Fig. 5g). This can be attributed to the fact that microtopography, such as hummocks and hollows, creates heterogeneity in hydrologic and thermal conditions as well as soil properties (e.g., moisture, enzyme activity, bulk density, or respiration), thereby influencing SOC stocks at a small scale (Iseas et al., 2024; Sullivan et al., 2008; Wang et al., 2021b; Wang et al., 2021c). We observed a negative correlation between terrain wetness index (TWI) and carbon stock (Table 2). In areas with high TWI, the soil is often saturated, creating anaerobic conditions that slow down carbon decomposition (Fenner and Freeman, 2011). While this can lead to peat formation over the long term, in the short term, it might mean that less new organic matter is added to the soil surface because the environment is less favourable for many types of plants that contribute to the surface carbon stock. Additionally, areas with higher TWI might experience more leaching or water flow, which could transport soluble organic carbon away from the topsoil, reducing the carbon stock. Elevation and slope control the water flow path, flow velocity, water accumulation, and runoff depth, which in turn affects carbon redistribution (Wiesmeier et al., 2019). For instance, steep slopes lead to higher water discharge and flow velocity, accelerating peat erosion and thus carbon redistribution (Graniero and Price, 1999). Therefore, the relatively smaller carbon stocks at the backslope may result from stronger erosion and hydrological dynamics due to the steeper slope.

Our results revealed a limited correlation between vegetation and carbon stocks across the landscape, which can be potentially attributed to the dual role of vegetation in carbon dynamics. This dual role encompasses the function of vegetation as a fresh carbon producer through photosynthesis (Pearson et al., 2013; Qian et al., 2010; Ward et al., 2013), as well as an old carbon promoter by altering peat soil nutrients and stimulating microorganism growth (Hartley et al., 2012; Lopatin et al., 2019; Walker et al., 2016). As a consequence, the interplay of fresh carbon production, old carbon decomposition, and water saturation level dynamics leads to a relatively complex or inconspicuous relationship between vegetation and carbon stocks in the short term (Lopatin et al., 2019). Moreover, their interactive effects may be modulated by vegetation types due to differences in net primary production, plant litter chemistry, and root biomass (Wiesmeier et al., 2019). In the Hautes Fagnes, peat Sphagnum moss produced decay-resistant litter that could reduce soil respiration (Dorrepaal et al., 2005) and thus played a crucial role in the rapid peat accumulation during the Atlantic, sub-boreal, and Sub-Atlantic periods (Frankard et al., 1998). However, owing to deep rooting and high transpiration, the invasion of *Molinia* disturbed the Hautes Fagnes peatland environment by increasing humic acid concentration and mineral content (Frankard et al., 1998). Consequently, it enhanced carbon decomposition and peat degradation processes (Ward et al., 2013), and led to the disappearance of typical peat-forming communities like *Sphagnum*. From our observations, *Molinia* has colonized almost everywhere except for the summit, in which vegetation cover is dominated by *Betula pubescens* and *Vaccinium myrtillus* (Fig. 1b). This can partly account for the large carbon inventory at the summit area.

Approximately 36 % of the spatial variation in SOC stock is not explained by existing factors, which we hypothesize may be due to spatial patterns of parent material. The impact of bedrock (e.g., permeability, mineral inputs, or soil texture) on soil carbon inventories has been reported in previous peatland studies (Chimner and Karberg, 2008; Hribljan et al., 2016; Shimada et al., 2001; Wang et al., 2021a). From our observations, the soils at the topslope positions developed on weathered quartzites are characterized by coarser soil texture (Table S3) and relatively high permeability (Henrion et al., 2024). However, soils in other areas, especially at the shoulder, developed on weathered shales or schists have fine texture (Table S3), smaller pore spaces, as well as a stable water table depth throughout the year. In addition, human disturbance may also play an important role. Drainage and conversion of peatlands to agriculture and forestry or other uses has led to a loss of capacity to store carbon (Leifeld and Menichetti, 2018; Minasny et al., 2023). In our study site, the long-term drainage for afforestation since the early 20th century might have influenced carbon storage. One of the most obvious effects of drainage is the increased aerobic decomposition of SOM in the drained layer, which subsequently leads to a rapid loss of peat and CO_2 emissions to the atmosphere, turning peatlands from carbon sinks into carbon sources (Minasny et al., 2023). Moreover, the presence of many ditches leads to a faster runoff flow rate and channel bank collapse, supplying large amounts of peat materials to the stream channel system (Holden et al., 2004). So far, many studies have reported that ditch erosion contributed to peat loss and increased suspended sediment yields (e.g., Li et al. (2018); Stenberg et al. (2015); Tuukkanen et al. (2016)). Erosion might be enhanced at the beginning of tree harvesting as vegetation cover plays a significant role in protecting peat from wind and water erosion (Li et al., 2018). These various processes

may have caused peat subsidence and carbon loss leading to an average SOC content within the peat horizon (37.47 ± 7.26 g/100 g) that is lower than that observed in western Canada (45.0 ± 4.3 g/100 g), the United States (48.9 ± 3.7 g/100 g), and the western European islands (54.0 ± 2.5 g/100 g) (Loisel et al., 2014).

4.2.2. SOC storage mapping and uncertainties

Model and variable selection is a critical step in the spatial prediction of SOC reservoirs. Crezee et al. (2022) mapped peat carbon stocks of the central Congo Basin by applying linear regressions between peat soil thickness and carbon stock ($R^2 = 0.86$, $n = 80$), which, however, is not suitable for our study case (Table 2). This is because they only considered the carbon stock within the peat horizon, while we estimated carbon storage of both the peat and mineral substrate within 1 m of the surface. Consequently, peat thickness could only explain 46 % of SOC stock variance in the multiple linear regressions (Table 2). A study conducted in an anthropogenic peatland in Chile showed that UAV-borne vegetation attributes such as vegetation height, species richness, and aboveground biomass were good predictors for carbon stock estimates (Lopatin et al., 2019). However, our findings indicate that current vegetation contributed only 16 % to the carbon stock spatial variability (Table 2). Hence, more environmental variables including peat thickness, three topographical features (elevation, TWI, and slope), and two vegetation attributes (CHM and OSAVI2) were considered as predictors. The random forest model was applied for mapping as it performed very well in the testing dataset ($R^2 = 0.85$, $RMSE = 59.3$ t/ha) when all variables were taken into account. We also tested the use of the multiple linear regression models for predictions. However, their performance in terms of R^2 and $RMSE$ were not as good as the Random Forest model, hence the results are not presented here.

Our results suggest that micro-topography explains more of the spatial variability in carbon stocks than macro-topography (Fig. 5g), and thus the use of high-resolution environmental variables enables carbon storage spatial mapping with high accuracy (Table 3, Fig. 6d). In a recent study, Fiantis et al. (2023) mapped carbon stocks using environmental variables derived from DEM (DEMNAS) data and Sentinel 1A satellite data, achieving only moderate prediction power ($R^2 = 0.39$). While satellite-derived data enables carbon storage estimation at large scales, the coarse resolution of satellite images smooths the heterogeneous surface at the landscape scale, thereby increasing the uncertainty of model predictions. In addition, our approach achieved robust carbon stock estimates across the landscape, which provides new insights for accurately mapping carbon inventories. Since subsurface carbon cannot be seen directly by traditional remote sensing technology, most previous studies relied on a predicted peat thickness map to estimate carbon stocks (e.g., Rudiyanto et al. (2016b), Rudiyanto et al. (2018), Akumu and McLaughlin (2014), Holden and Connolly (2011), Vernimmen et al. (2020)). Their carbon storage (in Mg) was calculated by multiplying the peat volume with carbon density. Peat volume was determined by summing the predicted peat thickness at all raster cells multiplied by cell area. Carbon density was based on average values of soil bulk density and carbon content from the literature. This methodology may introduce large uncertainties (Hribljan et al., 2017), as the carbon content and bulk density can vary significantly within the peat horizon, particularly in mountain peatlands (Hribljan et al., 2016).

However, peat thickness is the most important factor in our Random Forest model and, therefore, the largest source of uncertainty. Thus, the relatively large uncertainty of SOC stock prediction at the topslope and the floodplain is partly due to the uncertainty in peat thickness predictions at these slope positions (Fig. 6b, d). One way to improve mapping accuracy is to take more samples where these uncertainties are high (Bourgeau-Chavez et al., 2017). The GPR technology is a good option to accomplish this, as it allows for rapid determination of peat thickness with high spatial resolution (Henrion et al., 2024). Another source of uncertainty may arise from our sampling strategy. We took mixed soil samples within a 3 m diameter at 16 sites, while individual samples were collected at another 19 sites. Furthermore, when calculating carbon stocks of the top 1 m, we interpolated soil properties at sites sampled at depths of less than 1 m, which may have introduced bias.

5. Conclusions

In our study, the use of multi-sensor UAV data to map topography and vegetation, combined with a detailed characterization of the subsurface peat soil properties, enabled us to obtain a detailed 3D picture of peat thickness and SOC stocks at very high spatial resolution. Additionally, GPR provided key information regarding the continuous variation of peat thickness along a topographical gradient. By performing multiscale resolution analysis and multiple linear regressions, we successfully identified the relevant scales of topography to establish connections between surface and subsurface properties. To summarize, the main findings of our study are listed below:

(1) Peat thickness (range: 0.10–2.10 m, mean ± SD: 0.62 ± 0.37 m) and SOC stocks (range: 176.13–856.57 t/ha, mean ± SD: 539.14 ± 160.98 t/ha) show great spatial heterogeneity across the landscape.
(2) Peat thickness is strongly related to topographical features at macro-scales, which can explain more than 40 % of peat thickness spatial variability. The current vegetation types are a weaker predictor for peat thickness.
(3) In contrast, the SOC stock is more strongly controlled by micro-topography (21 %). Together, peat thickness, topography and vegetation can explain approximately 64 % of carbon storage variance.
(4) The different relevant spatial scales reflect the underlying processes. Macro-scale topographical features primarily influence peat thickness, shaping the large-scale accumulation of peat. Meanwhile, micro-topography affects SOC distribution by creating localized variations in moisture and temperature that influence decomposition rates. Understanding these scale-dependent processes is crucial for accurately modelling peatland carbon dynamics and predicting their responses to climate change.
(5) The UAV remote sensing data can yield robust spatial mapping of peat thickness and SOC stock, with $RMSE$ and R^2 values of 0.16 m and 0.85, respectively, for the peat thickness, and 59.3 t/ha and 0.85 for SOC stock. However, similar performance can also be achieved without considering data from the multispectral sensor. This demonstrates the great potential of UAVs for mapping, and eventually monitoring, peatland carbon reservoirs, but suggests that other types of sensors beyond LiDAR may offer minimal additional benefit.

CRediT authorship contribution statement

Yanfei Li: Writing – original draft, Visualization, Investigation, Formal analysis, Conceptualization. **Maud Henrion:** Writing – review & editing, Investigation. **Angus Moore:** Writing – review & editing. **Sébastien Lambot:** Writing – review & editing. **Sophie Opfergelt:** Writing – review & editing. **Veerle Vanacker:** Writing – review & editing. **François Jonard:** Writing – review & editing, Supervision, Funding acquisition, Conceptualization. **Kristof Van Oost:** Writing – review & editing, Supervision, Investigation, Funding acquisition, Conceptualization.

Declaration of competing interest

The authors declare that they have no known competing financial interests or personal relationships that could have appeared to influence the work reported in this paper.

Data availability

Data will be made available on request.

Acknowledgements

This work is an *Action de Recherche Concertée*, n° 21/26–119, funded by the *Communauté française de Belgique*. Yanfei Li wishes to thank the joint grant from China Scholarship Council and UCLouvain (No. 202106380030). Kristof Van Oost, Sophie Opfergelt, and Sébastien Lambot are supported by the *Fonds de la Recherche Scientifique* (FNRS). The authors would like to thank the *Département de la Nature et des Forêts* (DNF) and Joël Verdin for giving access to the study site. The authors would like to thank Dylan Vellut for his assistance with soil sampling and laboratory analysis.

Appendix A. Supplementary data

Supplementary data to this article can be found online at https://doi.org/10.1016/j.geoderma.2024.117009.

References

Aitkenhead, M.J., Coull, M.C., 2016. Mapping soil carbon stocks across Scotland using a neural network model. Geoderma 262, 187–198. https://doi.org/10.1016/j.geoderma.2015.08.034.

Akumu, C.E., McLaughlin, J.W., 2014. Modeling peatland carbon stock in a delineated portion of the Nayshkootayaow river watershed in Far North, Ontario using an integrated GIS and remote sensing approach. Catena 121, 297–306. https://doi.org/10.1016/j.catena.2014.05.025.

Aldana-Jague, E., Heckrath, G., Macdonald, A., van Wesemael, B., Van Oost, K., 2016. UAS-based soil carbon mapping using VIS-NIR (480–1000nm) multi-spectral imaging: Potential and limitations. Geoderma 275, 55–66. https://doi.org/10.1016/j.geoderma.2016.04.012.

Anda, M., Ritung, S., Suryani, E., Sukarman, Hikmat, M., Yatno, E., Mulyani, A., Subandiono, R.E., Suratman, Husnain, 2021. Revisiting tropical peatlands in Indonesia: Semi-detailed mapping, extent and depth distribution assessment. Geoderma 402, 115235. https://doi.org/10.1016/j.geoderma.2021.115235.

Bates, J.S., Montzka, C., Schmidt, M., Jonard, F., 2021. Estimating canopy density parameters time-series for winter wheat using UAS mounted LiDAR. Remote Sensing 13 (4), 710. https://doi.org/10.3390/rs13040710.

Beilman, D.W., Vitt, D.H., Bhatti, J.S., Forest, S., 2008. Peat carbon stocks in the southern Mackenzie River Basin: uncertainties revealed in a high-resolution case study. Global Change Biol. 14 (6), 1221–1232. https://doi.org/10.1111/j.1365-2486.2008.01565.x.

Beucher, A., Koganti, T., Iversen, B.V., Greve, M.H., 2020. Mapping of peat thickness using a multi-receiver electromagnetic induction instrument. Remote Sensing 12 (15), 2458. https://doi.org/10.3390/rs12152458.

Beuselinck, L., Govers, G., Poesen, J., Degraer, G., Froyen, L., 1998. Grain-size analysis by laser diffractometry: comparison with the sieve-pipette method. Catena 32 (3), 193–208. https://doi.org/10.1016/S0341-8162(98)00051-4.

Beyer, F., Jurasinski, G., Couwenberg, J., Grenzdörffer, G., 2019. Multisensor data to derive peatland vegetation communities using a fixed-wing unmanned aerial vehicle. Int. J. Remote Sens. 40 (24), 9103–9125. https://doi.org/10.1080/01431161.2019.1580825.

Beyer, F., Jansen, F., Jurasinski, G., Koch, M., Schröder, B., Koebsch, F., 2021. Drought years in peatland rewetting: rapid vegetation succession can maintain the net CO2 sink function. Biogeosciences 18 (3), 917–935. https://doi.org/10.5194/bg-18-917-2021.

Bjorke, J.T., Nilsen, S., 2003. Wavelets applied to simplification of digital terrain models. Int. J. Geograph. Inf. Sci. 17 (7), 601–621. https://doi.org/10.1080/1365881031000135500.

Böhner, J., Koethe, R., Conrad, O., Gross, J., Ringeler, A., Selige, T.J.S.C., 2001. Soil regionalisation by means of terrain analysis and process parameterisation. Soil Classification 7, 213.

Bourgeau-Chavez, L.L., Endres, S., Powell, R., Battaglia, M.J., Benscoter, B., Turetsky, M., Kasischke, E.S., Banda, E., 2017. Mapping boreal peatland ecosystem types from multitemporal radar and optical satellite imagery. Canadian J. Forest Res. 47 (4), 545–559. https://doi.org/10.1139/cjfr-2016-0192.

Breiman, L., 2001. Random forests. Mach. Learn. 45 (1), 5–32. https://doi.org/10.1023/A:1010933404324.

Carless, D., Luscombe, D.J., Gatis, N., Anderson, K., Brazier, R.E., 2019. Mapping landscape-scale peatland degradation using airborne lidar and multispectral data. Landscape Ecol. 34 (6), 1329–1345. https://doi.org/10.1007/s10980-019-00844-5.

Carless, D., Kulessa, B., Booth, A.D., Drocourt, Y., Sinnadurai, P., Street-Perrott, F.A., Jansson, P., 2021. An integrated geophysical and GIS based approach improves estimation of peatland carbon stocks. Geoderma 402, 115176. https://doi.org/10.1016/j.geoderma.2021.115176.

Chapman, S.J., Bell, J., Donnelly, D., Lilly, A., 2009. Carbon stocks in Scottish peatlands. Soil Use Manage. 25 (2), 105–112. https://doi.org/10.1111/j.1475-2743.2009.00219.x.

Chimner, R.A., Karberg, J.M., 2008. Long-term carbon accumulation in two tropical mountain peatlands, Andes Mountains, Ecuador. Mires Peat 3, 1–10.

Cobb, A.R., Dommain, R., Yeap, K., Hannan, C., Dadap, N.C., Bookhagen, B., Glaser, P.H., Harvey, C.F., 2024. A unified explanation for the morphology of raised peatlands. Nature 625 (7993), 79–84. https://doi.org/10.1038/s41586-023-06807-w.

Crezee, B., Dargie, G.C., Ewango, C.E.N., Mitchard, E.T.A., Emba, B.O., Kanyama, T.J., Bola, P., Ndjango, J.-B.N., Girkin, N.T., Bocko, Y.E., Ifo, S.A., Hubau, W., Seidensticker, D., Batumike, R., Imani, G., Cuní-Sanchez, A., Kiahtipes, C.A., Lebamba, J., Wotzka, H.-P., Bean, H., Baker, T.R., Baird, A.J., Boom, A., Morris, P.J., Page, S.E., Lawson, I.T., Lewis, S.L., 2022. Mapping peat thickness and carbon stocks of the central Congo Basin using field data. Nat. Geosci. 15 (8), 639–644. https://doi.org/10.1038/s41561-022-00966-7.

Czapiewski, S., 2022. Assessment of the applicability of UAV for the creation of digital surface model of a small peatland. Front. Earth Sci. 10 https://doi.org/10.3389/feart.2022.834923.

Czapiewski, S., Szumińska, D., 2022. An overview of remote sensing data applications in peatland research based on works from the period 2010–2021. Land 11 (1), 24. https://doi.org/10.3390/land11010024.

Dargie, G.C., Lewis, S.L., Lawson, I.T., Mitchard, E.T.A., Page, S.E., Bocko, Y.E., Ifo, S.A., 2017. Age, extent and carbon storage of the central Congo Basin peatland complex. Nature 542 (7639), 86–90. https://doi.org/10.1038/nature21048.

Davenport, I.J., McNicol, I., Mitchard, E.T.A., Dargie, G., Suspense, I., Milongo, B., Bocko, Y.E., Hawthorne, D., Lawson, I., Baird, A.J., Page, S., Lewis, S.L., 2020. First evidence of peat domes in the congo basin using LiDAR from a fixed-wing drone. Remote Sensing 12 (14), 2196. https://doi.org/10.3390/rs12142196.

Deragon, R., Saurette, D.D., Heung, B., Caron, J., 2022. Mapping the maximum peat thickness of cultivated organic soils in the southwest plain of Montreal. Canadian J. Soil Sci. 103 (1), 103–120. https://doi.org/10.1139/cjss-2022-0031.

Dettmann, U., Kraft, N.N., Rech, R., Heidkamp, A., Tiemeyer, B., 2021. Analysis of peat soil organic carbon, total nitrogen, soil water content and basal respiration: Is there a 'best' drying temperature? Geoderma 403, 115231. https://doi.org/10.1016/j.geoderma.2021.115231.

Dieleman, C.M., Branfireun, B.A., Lindo, Z., 2017. Northern peatland carbon dynamics driven by plant growth form — the role of graminoids. Plant Soil 415 (1), 25–35. https://doi.org/10.1007/s11104-016-3099-3.

Doolittle, J., 1987. Using ground-penetrating radar to increase the quality and efficiency of soil surveys. Soil Surv. Tech. 20, 11–32. https://doi.org/10.2136/sssaspecpub20.c2.

Dorrepaal, E., Cornelissen, J.H.C., Aerts, R., WallÉN, B.O., Van Logtestijn, R.S.P., 2005. Are growth forms consistent predictors of leaf litter quality and decomposability across peatlands along a latitudinal gradient? J. Ecol. 93 (4), 817–828. https://doi.org/10.1111/j.1365-2745.2005.01024.x.

Dorrepaal, E., Toet, S., van Logtestijn, R.S.P., Swart, E., van de Weg, M.J., Callaghan, T.V., Aerts, R., 2009. Carbon respiration from subsurface peat accelerated by climate warming in the subarctic. Nature 460 (7255), 616–619. https://doi.org/10.1038/nature08216.

Farmer, J., Matthews, R., Smith, P., Langan, C., Hergoualc'h, K., Verchot, L., Smith, J.U., 2014. Comparison of methods for quantifying soil carbon in tropical peats. Geoderma 214–215, 177–183. https://doi.org/10.1016/j.geoderma.2013.09.013.

Fenner, N., Freeman, C., 2011. Drought-induced carbon loss in peatlands. Nat. Geosci. 4 (12), 895–900. https://doi.org/10.1038/ngeo1323.

Fernandes, M.R., Aguiar, F.C., Martins, M.J., Rico, N., Ferreira, M.T., Correia, A.C., 2020. Carbon stock estimations in a mediterranean riparian forest: A case study combining field data and UAV imagery. Forests 11 (4), 376. https://doi.org/10.3390/f11040376.

Fiantis, D., Rudiyanto, Ginting, F.I., Agtalarik, A., Arianto, D.T., Wichaksono, P., Irfan, R., Nelson, M., Gusnidar, G., Jeon, S., Minasny, B., 2023. Mapping peat thickness and carbon stock of a degraded peatland in West Sumatra, Indonesia. Soil Use Manage. https://doi.org/10.1111/sum.12954.

Fox, J., Monette, G., 1992. Generalized collinearity diagnostics. J. Am. Stat. Assoc. 87 (417), 178–183. https://doi.org/10.2307/2290467.

Frankard, P., Ghiette, P., Hindryckx, M.-N., Schumacker, R., Wastiaux, C., 1998. Peatlands of Wallony (S-Belgium). Journal 49 (2), 33–37.

Gatis, N., Luscombe, D.J., Carless, D., Parry, L.E., Fyfe, R.M., Harrod, T.R., Brazier, R.E., Anderson, K., 2019. Mapping upland peat depth using airborne radiometric and lidar survey data. Geoderma 335, 78–87. https://doi.org/10.1016/j.geoderma.2018.07.041.

Goemaere, E., Demarque, S., Dreesen, R., Declercq, P.-Y., 2016. The geological and cultural heritage of the caledonian Stavelot-Venn Massif. Belgium. Geoheritage 8 (3), 211–233. https://doi.org/10.1007/s12371-015-0155-y.

Gorham, E., 1957. The development of peat lands. Quart. Rev. Biol. 32 (2), 145–166.

Graniero, P.A., Price, J.S., 1999. The importance of topographic factors on the distribution of bog and heath in a Newfoundland blanket bog complex. Catena 36 (3), 233–254. https://doi.org/10.1016/S0341-8162(99)00008-9.

Hair, J., Black, W., Babin, B., Anderson, R., 2010. Multivariate Data Analysis: A Global Perspective.

Harris, A., Baird, A.J., 2019. Microtopographic drivers of vegetation patterning in blanket peatlands recovering from erosion. Ecosystems 22 (5), 1035–1054. https://doi.org/10.1007/s10021-018-0321-6.

Harris, A., Charnock, R., Lucas, R.M., 2015. Hyperspectral remote sensing of peatland floristic gradients. Remote Sens. Environ. 162, 99–111. https://doi.org/10.1016/j.rse.2015.01.029.

Hartley, I.P., Garnett, M.H., Sommerkorn, M., Hopkins, D.W., Fletcher, B.J., Sloan, V.L., Phoenix, G.K., Wookey, P.A., 2012. A potential loss of carbon associated with greater plant growth in the European Arctic. Nat. Clim. Change 2 (12), 875–879. https://doi.org/10.1038/nclimate1575.

Henrich, V., Götze, C., Jung, A., Sandow, C., Thürkow, D., Cornelia, G., 2009. Development of an online indices database: Motivation, concept and implementation.

Henrion, M., Li, Y., Koganti, T., Bechtold, M., Jonard, F., Opfergelt, S., Vanacker, V., Van Oost, K., Lambot, S., 2024. Mapping and monitoring peatlands in the Belgian Hautes Fagnes: Insights from Ground-penetrating radar and Electromagnetic induction characterization. Geoderma Regional 37, e00795.

Holden, J., Chapman, P.J., Labadz, J.C., 2004. Artificial drainage of peatlands: hydrological and hydrochemical process and wetland restoration. Prog. Phys. Geogr.: Earth Environ. 28 (1), 95–123. https://doi.org/10.1191/0309133304pp403ra.

Holden, N.M., Connolly, J., 2011. Estimating the carbon stock of a blanket peat region using a peat depth inference model. Catena 86 (2), 75–85. https://doi.org/10.1016/j.catena.2011.02.002.

Houbrechts, G., Petit, F., Van Campenhout, J., Juvigné, E., Demoulin, A., 2018. A unique boulder-bed reach of the amblève river, ardenne, at fonds de quarreux: modes of boulder transport. In: Demoulin, A. (Ed.), Landscapes and Landforms of Belgium and Luxembourg. Springer International Publishing, Cham, pp. 85–99.

Hribljan, J.A., Suárez, E., Heckman, K.A., Lilleskov, E.A., Chimner, R.A., 2016. Peatland carbon stocks and accumulation rates in the Ecuadorian páramo. Wetlands Ecol. Manage. 24 (2), 113–127. https://doi.org/10.1007/s11273-016-9482-2.

Hribljan, J.A., Suarez, E., Bourgeau-Chavez, L., Endres, S., Lilleskov, E.A., Chimbolema, S., Wayson, C., Serocki, E., Chimner, R.A., 2017. Multidate, multisensor remote sensing reveals high density of carbon-rich mountain peatlands in the páramo of Ecuador. Global Change Biol. 23 (12), 5412–5425. https://doi.org/10.1111/gcb.13807.

Huang, Y., Ciais, P., Luo, Y., Zhu, D., Wang, Y., Qiu, C., Goll, D.S., Guenet, B., Makowski, D., De Graaf, I., Leifeld, J., Kwon, M.J., Hu, J., Qu, L., 2021. Tradeoff of CO2 and CH4 emissions from global peatlands under water-table drawdown. Nat. Climate Change 11 (7), 618–622. https://doi.org/10.1038/s41558-021-01059-w.

Illés, G., Sutikno, S., Szatmári, G., Sandhyavitri, A., Pásztor, L., Kristijono, A., Molnár, G., Yusa, M., Székely, B., 2019. Facing the peat CO2 threat: digital mapping of Indonesian peatlands—a proposed methodology and its application. J. Soils Sediments 19 (11), 3663–3678. https://doi.org/10.1007/s11368-019-02328-0.

Iseas, M.S., Rossi, M.F., Aravena Acuña, M.-C., Pancotto, V.A., 2024. Influence of the microtopography of patagonian peatbogs on the fluxes of greenhouse gasses and dissolved carbon in porewater. Ecohydrol. Hydrobiol. https://doi.org/10.1016/j.ecohyd.2024.01.013.

Jaenicke, J., Rieley, J.O., Mott, C., Kimman, P., Siegert, F., 2008. Determination of the amount of carbon stored in Indonesian peatlands. Geoderma 147 (3), 151–158. https://doi.org/10.1016/j.geoderma.2008.08.008.

Jonard, F., Bircher, S., Demontoux, F., Weihermüller, L., Razafindratsima, S., Wigneron, J.-P., Vereecken, H., 2018. Passive L-band microwave remote sensing of organic soil surface layers: A tower-based experiment. Remote Sensing 10 (2), 304. https://doi.org/10.3390/rs10020304.

Joosten, H., Clarke, D., 2002. Wise use of mires and peatlands. International Mire Conservation Group, p. 304.

Kalbermatten, M., Van De Ville, D., Turberg, P., Tuia, D., Joost, S., 2012. Multiscale analysis of geomorphological and geological features in high resolution digital elevation models using the wavelet transform. Geomorphology 138 (1), 352–363. https://doi.org/10.1016/j.geomorph.2011.09.023.

Keaney, A., McKinley, J., Graham, C., Robinson, M., Ruffell, A., 2013. Spatial statistics to estimate peat thickness using airborne radiometric data. Spatial Stat. 5, 3–24. https://doi.org/10.1016/j.spasta.2013.05.003.

Koganti, T., Vigah Adetsu, D., Triantafilis, J., Greve, M.H., Beucher, A.M., 2023. Mapping peat depth using a portable gamma-ray sensor and terrain attributes. Geoderma 439, 116672. https://doi.org/10.1016/j.geoderma.2023.116672.

Krüger, J.P., Dotterweich, M., Seifert-Schäfer, A., Hoffmann, S., Kopf, C., Kneisel, C., Dotzler, S., Nink, S., Stoffels, J., Schueler, G., 2021. Carbon stocks and their spatial distribution in drained and rewetted peatland forests in a low mountain range area, Germany. Mires and Peat 27. https://doi.org/10.19189/MaP.2020.BG.StA.1991.

Lashermes, B., Foufoula-Georgiou, E., Dietrich, W.E., 2007. Channel network extraction from high resolution topography using wavelets. Geophys. Res. Lett. 34 (23), L23S04. https://doi.org/10.1029/2007GL031140.

Leifeld, J., Menichetti, L., 2018. The underappreciated potential of peatlands in global climate change mitigation strategies. Nat. Commun. 9 (1), 1071. https://doi.org/10.1038/s41467-018-03406-6.

Leng, L.Y., Ahmed, O.H., Jalloh, M.B., 2019. Brief review on climate change and tropical peatlands. Geosci. Front. 10 (2), 373–380. https://doi.org/10.1016/j.gsf.2017.12.018.

Li, C., Grayson, R., Holden, J., Li, P., 2018. Erosion in peatlands: Recent research progress and future directions. Earth-Sci. Rev. 185, 870–886. https://doi.org/10.1016/j.earscirev.2018.08.005.

Loisel, J., van Bellen, S., Pelletier, L., Talbot, J., Hugelius, G., Karran, D., Yu, Z., Nichols, J., Holmquist, J., 2017. Insights and issues with estimating northern peatland carbon stocks and fluxes since the Last Glacial Maximum. Earth-Sci. Rev. 165, 59–80. https://doi.org/10.1016/j.earscirev.2016.12.001.

Lopatin, J., Kattenborn, T., Galleguillos, M., Perez-Quezada, J.F., Schmidtlein, S., 2019. Using aboveground vegetation attributes as proxies for mapping peatland belowground carbon stocks. Remote Sens. Environ. 231, 111217 https://doi.org/10.1016/j.rse.2019.111217.

Lovitt, J., Rahman, M.M., McDermid, G.J., 2017. Assessing the value of UAV photogrammetry for characterizing terrain in complex peatlands. Remote Sensing 9 (7), 715. https://doi.org/10.3390/rs9070715.

Loisel, J., Yu, Z., Beilman, D.W., Camill, P., Alm, J., Amesbury, M.J., Anderson, D., Andersson, S., Bochicchio, C., Barber, K., Belyea, L.R., Bunbury, J., Chambers, F.M., Charman, D.J., De Vleeschouwer, F., Fiałkiewicz-Kozieł, B., Finkelstein, S.A., Gałka, M., Garneau, M., Hammarlund, D., Hinchcliffe, W., Holmquist, J., Hughes, P., Jones, M.C., Klein, E.S., Kokfelt, U., Korhola, A., Kuhry, P., Lamarre, A., Lamentowicz, M., Large, D., Lavoie, M., MacDonald, G., Magnan, G., Mäkilä, M., Mallon, G., Mathijssen, P., Mauquoy, D., McCarroll, J., Moore, T.R., Nichols, J., O'Reilly, B., Oksanen, P., Packalen, M., Peteet, D., Richard, P.J.H., Robinson, S., Ronkainen, T., Rundgren, M., Sannel, A.B.K., Tarnocai, C., Thom, T., Tuittila, E.-S., Turetsky, M., Väliranta, M., van der Linden, M., van Geel, B., van Bellen, S., Vitt, D., Zhao, Y., Zhou, W., 2014. A database and synthesis of northern peatland soil properties and Holocene carbon and nitrogen accumulation. The Holocene 24 (9), 1028–1042. https://doi.org/10.1177/0959683614538073.

MacKenzie, D.I., Nichols, J.D., Lachman, G.B., Droege, S., Andrew Royle, J., Langtimm, C.A., 2002. Estimating site occupancy rates when detection probabilities are less than one. Ecology 83 (8), 2248–2255. https://doi.org/10.1890/0012-9658(2002)083[2248:ESORWD]2.0.CO;2.

Malone, B.P., McBratney, A.B., Minasny, B., 2011. Empirical estimates of uncertainty for mapping continuous depth functions of soil attributes. Geoderma 160 (3), 614–626. https://doi.org/10.1016/j.geoderma.2010.11.013.

McClellan, M., Comas, X., Benscoter, B., Hinkle, R., Sumner, D., 2017. Estimating belowground carbon stocks in isolated wetlands of the Northern Everglades watershed, Central Florida, using ground penetrating radar and aerial imagery. J. Geophys. Res. Biogeosci. 122 (11), 2804–2816. https://doi.org/10.1002/2016JG003573.

Mestdagh, I., Sleutel, S., Lootens, P., Van Cleemput, O., Beheydt, D., Boeckx, P., De Neve, S., Hofman, G., Van Camp, N., Vande Walle, I., Samson, R., Verheyen, K., Lemeur, R., Carlier, L., 2009. Soil organic carbon–stock changes in Flemish grassland soils from 1990 to 2000. J. Plant Nutr. Soil Sci. 172 (1), 24–31. https://doi.org/10.1002/jpln.200700132.

Minasny, B., Berglund, Ö., Connolly, J., Hedley, C., de Vries, F., Gimona, A., Kempen, B., Kidd, D., Lilja, H., Malone, B., McBratney, A., Roudier, P., O'Rourke, S., Rudiyanto, Padarian, J., Poggio, L., ten Caten, A., Thompson, D., Tuve, C., Widyatmanti, W., 2019. Digital mapping of peatlands – A critical review. Earth-Sci. Rev. 196, 102870 https://doi.org/10.1016/j.earscirev.2019.05.014.

Minasny, B., Adetsu, D.V., Aitkenhead, M., Artz, R.R.E., Baggaley, N., Barthelmes, A., Beucher, A., Caron, J., Conchedda, G., Connolly, J., Deragon, R., Evans, C., Fadnes, K., Fiantis, D., Gagkas, Z., Gilet, L., Gimona, A., Glatzel, S., Greve, M.H., Habib, W., Hergoualc'h, K., Hermansen, C., Kidd, D.B., Koganti, T., Kopansky, D., Large, D.J., Larmola, T., Lilly, A., Liu, H., Marcus, M., Middleton, M., Morrison, K., Petersen, R.J., Quaife, T., Rochefort, L., Rochefort, L., Rudiyanto, Toca, L., Tubiello, F.N., Weber, P.L., Weldon, S., Widyatmanti, W., Williamson, J., Zak, D., 2023. Mapping and monitoring peatland conditions from global to field scale. Biogeochemistry 167, 383–425. https://doi.org/10.1007/s10533-023-01084-1.

Moore, P.D., 1989. The ecology of peat-forming processes: a review. Int. J. Coal Geol. 12 (1), 89–103. https://doi.org/10.1016/0166-5162(89)90048-7.

Moore, I.D., Lewis, A., Gallant, J.C., 1993. Terrain attributes: estimation methods and scale effects, pp. 189-214.

Mormal, P., Tricot, C., 2004. Aperçu climatique des Hautes-Fagnes, Institut Royal météorologique de Belgique.

Mosteller, F., Tukey, J., 1968. Data analysis, including statistics. In: Lindzey, G., Aronson, E. (Eds.), Revised Handbook of Social Psychology. Addison Wesley, pp. 80–203.

Murdoch, D.J., Chow, E.D., 1996. A graphical display of large correlation matrices. Am. Statis. 50 (2), 178–180. https://doi.org/10.2307/2684435.

Nissan, A., Alcolombri, U., Peleg, N., Galili, N., Jimenez-Martinez, J., Molnar, P., Holzner, M., 2023. Global warming accelerates soil heterotrophic respiration. Nat. Commun. 14 (1), 3452. https://doi.org/10.1038/s41467-023-38981-w.

Orella, J., Africa, D.R., Bustillo, C.H., Pascua, N., Marquez, C., Adornado, H., Aguilos, M., 2022. Above-and-belowground carbon stocks in two contrasting peatlands in the Philippines. Forests 13 (2), 303. https://doi.org/10.3390/f13020303.

Palozzi, J.E., Lindo, Z., 2017. Boreal peat properties link to plant functional traits of ecosystem engineers. Plant Soil 418 (1), 277–291. https://doi.org/10.1007/s11104-017-3291-0.

Pan, Y., Birdsey, R.A., Fang, J., Houghton, R., Kauppi, P.E., Kurz, W.A., Phillips, O.L., Shvidenko, A., Lewis, S.L., Canadell, J.G., Ciais, P., Jackson, R.B., Pacala, S.W., McGuire, A.D., Piao, S., Rautiainen, A., Sitch, S., Hayes, D., 2011. A large and persistent carbon sink in the world's forests. Science 333 (6045), 988–993. https://doi.org/10.1126/science.1201609.

Parry, L.E., Charman, D.J., Noades, J.P.W., 2012. A method for modelling peat depth in blanket peatlands. Soil Use Manage. 28 (4), 614–624. https://doi.org/10.1111/j.1475-2743.2012.00447.x.

Parry, L.E., Charman, D.J., 2013. Modelling soil organic carbon distribution in blanket peatlands at a landscape scale. Geoderma 211–212, 75–84. https://doi.org/10.1016/j.geoderma.2013.07.006.

Parry, L.E., West, L.J., Holden, J., Chapman, P.J., 2014. Evaluating approaches for estimating peat depth. J. Geophys. Res. Biogeosci. 119 (4), 567–576. https://doi.org/10.1002/2013JG002411.

Pearson, R.G., Phillips, S.J., Loranty, M.M., Beck, P.S.A., Damoulas, T., Knight, S.J., Goetz, S.J., 2013. Shifts in Arctic vegetation and associated feedbacks under climate change. Nat. Clim. Change 3 (7), 673–677. https://doi.org/10.1038/nclimate1858.

Pissart, A., 2003. The remnants of Younger Dryas lithalsas on the Hautes Fagnes Plateau in Belgium and elsewhere in the world. Geomorphology 52 (1), 5–38. https://doi.org/10.1016/S0169-555X(02)00246-5.
Plunus, J., Loute, M., Mackels, D., Arens, D., Dumoulin, V., 2013. Restauration des landes et tourbières du Plateau des Hautes Fagnes.
Qian, H., Joseph, R., Zeng, N., 2010. Enhanced terrestrial carbon uptake in the northern high latitudes in the 21st century from the coupled carbon cycle climate model intercomparison project model projections. Global Change Biol. 16 (2), 641–656. https://doi.org/10.1111/j.1365-2486.2009.01989.x.
Räsänen, A., Aurela, M., Juutinen, S., Kumpula, T., Lohila, A., Penttilä, T., Virtanen, T., 2020. Detecting northern peatland vegetation patterns at ultra-high spatial resolution. Remote Sens. Ecol. Conserv. 6 (4), 457–471. https://doi.org/10.1002/rse2.140.
Räsänen, A., Virtanen, T., 2019. Data and resolution requirements in mapping vegetation in spatially heterogeneous landscapes. Remote Sens. Environ. 230, 111207 https://doi.org/10.1016/j.rse.2019.05.026.
Rodriguez, A.F., Gerber, S., Inglett, P.W., Tran, N.T., Long, J.R., Daroub, S.H., 2021. Soil carbon characterization in a subtropical drained peatland. Geoderma 382, 114758. https://doi.org/10.1016/j.geoderma.2020.114758.
Rudiyanto, Minasny, B., Setiawan, B.I., 2016a. Further results on comparison of methods for quantifying soil carbon in tropical peats. Geoderma 269, 108–111. https://doi.org/10.1016/j.geoderma.2016.01.038.
Rudiyanto, Minasny, B., Setiawan, B.I., Arif, C., Saptomo, S.K., Chadirin, Y., 2016b. Digital mapping for cost-effective and accurate prediction of the depth and carbon stocks in Indonesian peatlands. Geoderma 272, 20–31. https://doi.org/10.1016/j.geoderma.2016.02.026.
Rudiyanto, Minasny, B., Setiawan, B.I., Saptomo, S.K., McBratney, A.B., 2018. Open digital mapping as a cost-effective method for mapping peat thickness and assessing the carbon stock of tropical peatlands. Geoderma 313, 25–40. https://doi.org/10.1016/j.geoderma.2017.10.018.
Rudiyanto, Setiawan, B.I., Arief, C., Saptomo, S.K., Gunawan, A., Kuswarman, Sungkono, Indriyanto, H., 2015. Estimating distribution of carbon stock in tropical peatland using a combination of an empirical peat depth model and GIS. Procedia Environ. Sci. 24, 152–157. https://doi.org/10.1016/j.proenv.2015.03.020.
Rydin, H., 2013. The biology of peatlands. The biology of habitats series, 2nd ed. Oxford University Press, Oxford.
Shimada, S., Takahashi, H., Haraguchi, A., Kaneko, M., 2001. The carbon content characteristics of tropical peats in Central Kalimantan, Indonesia: Estimating their spatial variability in density. Biogeochemistry 53, 249–267. https://doi.org/10.1023/A:1010618807469.
Shukla, T., Tang, W., Trettin, C.C., Chen, G., Chen, S., Allan, C., 2023. Quantification of microtopography in natural ecosystems using close-range remote sensing. Remote Sens. 15 (9), 2387. https://doi.org/10.3390/rs15092387.
Silvestri, S., Christensen, C.W., Lysdahl, A.O.K., Anschütz, H., Pfaffhuber, A.A., Viezzoli, A., 2019a. Peatland volume mapping over resistive substrates with airborne electromagnetic technology. Geophys. Res. Lett. 46 (12), 6459–6468. https://doi.org/10.1029/2019GL083025.
Silvestri, S., Knight, R., Viezzoli, A., Richardson, C.J., Anshari, G.Z., Dewar, N., Flanagan, N., Comas, X., 2019b. Quantification of peat thickness and stored carbon at the landscape scale in tropical peatlands: A comparison of airborne geophysics and an empirical topographic method. J. Geophys. Res.. Earth Surf. 1294 (12), 3107–3123. https://doi.org/10.1029/2019JF005273.
Sleutel, S., De Neve, S., Hofman, G., 2003. Estimates of carbon stock changes in Belgian cropland. Soil Use Manage. 19 (2), 166–171. https://doi.org/10.1111/j.1475-2743.2003.tb00299.x.
Sougnez, N., Vanacker, V., 2011. The topographic signature of Quaternary tectonic uplift in the Ardennes massif (Western Europe). Hydrol. Earth Syst. Sci. 15 (4), 1095–1107. https://doi.org/10.5194/hess-15-1095-2011.
Stenberg, L., Tuukkanen, T., Finér, L., Marttila, H., Piirainen, S., Kløve, B., Koivusalo, H., 2015. Ditch erosion processes and sediment transport in a drained peatland forest. Ecol. Eng. 75, 421–433. https://doi.org/10.1016/j.ecoleng.2014.11.046.
Sullivan, P.F., Arens, S.J.T., Chimner, R.A., Welker, J.M., 2008. Temperature and microtopography interact to control carbon cycling in a high Arctic Fen. Ecosystems 11 (1), 61–76. https://doi.org/10.1007/s10021-007-9107-y.
Sutton-Grier, A.E., Megonigal, J.P., 2011. Plant species traits regulate methane production in freshwater wetland soils. Soil Biol. Biochem. 43 (2), 413–420. https://doi.org/10.1016/j.soilbio.2010.11.009.
Tonks, A.J., Aplin, P., Beriro, D.J., Cooper, H., Evers, S., Vane, C.H., Sjögersten, S., 2017. Impacts of conversion of tropical peat swamp forest to oil palm plantation on peat organic chemistry, physical properties and carbon stocks. Geoderma 289, 36–45. https://doi.org/10.1016/j.geoderma.2016.11.018.
van der Velde, Y., Temme, A.J.A.M., Nijp, J.J., Braakhekke, M.C., van Voorn, G.A.K., Dekker, S.C., Dolman, A.J., Wallinga, J., Devito, K.J., Kettridge, N., Mendoza, C.A., Kooistra, L., Soons, M.B., Teuling, A.J., 2021. Emerging forest–peatland bistability and resilience of European peatland carbon stores. Proc. Natl. Acad. Sci. 118(38), e2101742118. https://doi.org/10.1073/pnas.2101742118.
Tuukkanen, T., Stenberg, L., Marttila, H., Finér, L., Piirainen, S., Koivusalo, H., Kløve, B., 2016. Erosion mechanisms and sediment sources in a peatland forest after ditch cleaning. Earth Surface Processes and Landforms 41 (13), 1841–1853. https://doi.org/10.1002/esp.3951.
Vernimmen, R., Hooijer, A., Akmalia, R., Fitranatanegara, N., Mulyadi, D., Yuherdha, A., Andreas, H., Page, S., 2020. Mapping deep peat carbon stock from a LiDAR based DTM and field measurements, with application to eastern Sumatra. Carbon Balance Manage. 15 (1), 4. https://doi.org/10.1186/s13021-020-00139-2.
Veron, P., Bah, B., Bracke, C., Lejeune, P., Rondeux, J., Bock, L., Mokadem, A.I., 2005. The digital soil map of Wallonia (DSMW/CNSW), XXII International Cartographic Conference (ICC2005), A Coruña, Spain, pp. 8.
Villa, J.A., Mejía, G.M., Velásquez, D., Botero, A., Acosta, S.A., Marulanda, J.M., Osorno, A.M., Bohrer, G., 2019. Carbon sequestration and methane emissions along a microtopographic gradient in a tropical Andean peatland. Sci. Total Environ. 654, 651–661. https://doi.org/10.1016/j.scitotenv.2018.11.109.
Walker, J.S., 2019. A Primer on Wavelets and Their Scientific Applications. CRC Press.
Walker, T.N., Garnett, M.H., Ward, S.E., Oakley, S., Bardgett, R.D., Ostle, N.J., 2016. Vascular plants promote ancient peatland carbon loss with climate warming. Global Change Biol. 22 (5), 1880–1889. https://doi.org/10.1111/gcb.13213.
Walle, I., Camp, N., Perrin, D., Lemeur, R., Verheyen, K., Wesemael, B., Laitat, E., 2005. Growing stock-based assessment of the carbon stock in the Belgian forest biomass. Ann. Forest Sci. 62 (8), 853–864. https://doi.org/10.1051/forest:2005076.
Wang, S., Zhuang, Q., Lähteenoja, O., Draper, F.C., Cadillo-Quiroz, H., 2018. Potential shift from a carbon sink to a source in Amazonian peatlands under a changing climate. Proc. Natl. Acad. Sci. 115(49), 12407-12412. https://doi.org/10.1073/pnas.1801317115.
Wang, M., Han, Y., Xu, Z., Wang, S., Jiang, M., Wang, G., 2021b. Hummock-hollow microtopography affects soil enzyme activity by creating environmental heterogeneity in the sedge-dominated peatlands of the Changbai Mountains, China. Ecol. Indicat. 121, 107187 https://doi.org/10.1016/j.ecolind.2020.107187.
Wang, M., Wang, S., Cao, Y., Jiang, M., Wang, G., Dong, Y., 2021c. The effects of hummock-hollow microtopography on soil organic carbon stocks and soil labile organic carbon fractions in a sedge peatland in Changbai Mountain, China. CATENA 201, 105204. https://doi.org/10.1016/j.catena.2021.105204.
Wang, M., Liu, H., Rezanezhad, F., Zak, D., Lennartz, B., 2023. The influence of microtopography on soil carbon accumulation and nutrient release from a rewetted coastal peatland. Geoderma 438, 116637. https://doi.org/10.1016/j.geoderma.2023.116637.
Wang, D., Zang, S., Wu, X., Ma, D., Li, M., Chen, Q., Liu, X., Zhang, N., 2021a. Soil organic carbon stabilization in permafrost peatlands. Saudi J. Biol. Sci. 28 (12), 7037–7045. https://doi.org/10.1016/j.sjbs.2021.07.088.
Ward, S.E., Ostle, N.J., Oakley, S., Quirk, H., Henrys, P.A., Bardgett, R.D., 2013. Warming effects on greenhouse gas fluxes in peatlands are modulated by vegetation composition. Ecol. Lett. 16 (10), 1285–1293. https://doi.org/10.1111/ele.12167.
Warren, M., Hergoualc'h, K., Kauffman, J.B., Murdiyarso, D., Kolka, R., 2017. An appraisal of Indonesia's immense peat carbon stock using national peatland maps: uncertainties and potential losses from conversion. Carbon Balance Manage. 12 (1), 12. https://doi.org/10.1186/s13021-017-0080-2.
Wastiaux, C., Halleux, L., Schumacker, R., Streel, M., Jacqmotte, J., 2000. Development of the Hautes-Fagnes peat bogs (Belgium): New perspectives using ground-penetrating radar. Journal 51 (3), 115–120.
Wiesmeier, M., Urbanski, L., Hobley, E., Lang, B., von Lützow, M., Marin-Spiotta, E., van Wesemael, B., Rabot, E., Ließ, M., Garcia-Franco, N., Wollschläger, U., Vogel, H.-J., Kögel-Knabner, I., 2019. Soil organic carbon storage as a key function of soils - A review of drivers and indicators at various scales. Geoderma 333, 149–162. https://doi.org/10.1016/j.geoderma.2018.07.026.
Wilkinson, S.L., Andersen, R., Moore, P.A., Davidson, S.J., Granath, G., Waddington, J. M., 2023. Wildfire and degradation accelerate northern peatland carbon release. Nat. Clim. Change 13 (5), 456–461. https://doi.org/10.1038/s41558-023-01657-w.
Wilkinson, G.N., Rogers, C.E., 1973. Symbolic description of factorial models for analysis of variance. J. R. Stat. Soc.: Ser. C (Applied Statistics) 22 (3), 392–399. https://doi.org/10.2307/2346786.
Wood, J., 1996. The geomorphological characterisation of Digital Elevation Models. University of Leicester, U.K.
Wood, J., 2009. Geomorphometry in LandSerf Developments in Soil Science. In: T. Hengl, H. Reuter (Eds.), Geomorphometry. Concepts, Software, Applications. Elsevier, Armsterdam, pp. 333-349.
Xu, J., Morris, P.J., Liu, J., Holden, J., 2018. PEATMAP: Refining estimates of global peatland distribution based on a meta-analysis. Catena 160, 134–140. https://doi.org/10.1016/j.catena.2017.09.010.
Young, D.M., Parry, L.E., Lee, D., Ray, S., 2018. Spatial models with covariates improve estimates of peat depth in blanket peatlands. PLoS One 13 (9), e0202691.
Yu, Z.C., 2012. Northern peatland carbon stocks and dynamics: a review. Biogeosciences 9 (10), 4071–4085. https://doi.org/10.5194/bg-9-4071-2012.
Yu, Z., Loisel, J., Brosseau, D.P., Beilman, D.W., Hunt, S.J., 2010. Global peatland dynamics since the Last Glacial Maximum. Geophys. Res. Lett. 37 (13) https://doi.org/10.1029/2010GL043584.
Zhao, P., Fallu, D.J., Pears, B.R., Allonsius, C., Lembrechts, J.J., Van de Vondel, S., Meysman, F.J.R., Cucchiaro, S., Tarolli, P., Shi, P., Six, J., Brown, A.G., van Wesemael, B., Van Oost, K., 2023. Quantifying soil properties relevant to soil organic carbon biogeochemical cycles by infrared spectroscopy: The importance of compositional data analysis. Soil Tillage Res. 231, 105718 https://doi.org/10.1016/j.still.2023.105718.
Zhao, J., Peichl, M., Nilsson, M.B., 2017. Long-term enhanced winter soil frost alters growing season CO2 fluxes through its impact on vegetation development in a boreal peatland. Global Change Biol. 23 (8), 3139–3153. https://doi.org/10.1111/gcb.13621.
Zhou, Y., Chartin, C., Van Oost, K., van Wesemael, B., 2022. High-resolution soil organic carbon mapping at the field scale in Southern Belgium (Wallonia). Geoderma 422, 115929. https://doi.org/10.1016/j.geoderma.2022.115929.